
Article:
Wang, Y, Fairweather, M, Mortimer, LF orcid.org/0000-0002-4243-956X et al. (2 more authors) (2020) Mechanisms of particle preferential concentration induced by secondary motions in a dilute turbulent square duct flow. Physics of Fluids, 32 (12). 123313. ISSN 1070-6631

https://doi.org/10.1063/5.0032472

Mechanisms of particle preferential concentration induced by secondary motions in a dilute turbulent square duct flow

Y. Wang[1,2], M. Fairweather[2], L.F. Mortimer[2], Y. Zhao[1] and J. Yao[1]

[1] Beijing Key Laboratory of Process Fluid Filtration and Separation, College of Mechanical and Transportation Engineering, China University of Petroleum-Beijing, Beijing 102249, PR China

[2] School of Chemical and Process Engineering, University of Leeds, Leeds, LS2 9JT, UK

ABSTRACT

Particle-laden turbulent square duct flows at $Re_\tau = 300$ (based on the duct half-width and the mean friction velocity) are investigated using direct numerical simulation with one- and two-way coupled Lagrangian particle tracking. Four particle-to-fluid density ratios are considered with the corresponding shear Stokes number St^+ = 0.31, 25, 125 and 260. Particle motion is governed by drag, lift, virtual mass and pressure gradient forces. The main purpose of this work is to examine the effect of the turbulence-driven secondary flows on particle preferential accumulation, as well as its dependence on Stokes number. Results obtained indicate that the cross-stream secondary motions encourage inertial particles to accumulate preferentially in the duct corners, where the maximum of the cross-sectional particle concentration occurs. The extent of accumulation here is strongly dependent on Stokes number, with the greatest accumulation found at St^+=25. Interestingly, the maximum of the intensity of the secondary particle velocity along the corner bisector is also achieved at $St^+ = 25$, whereas in the region adjacent to the wall, it is found to decrease with particle Stokes number. Additionally, it is observed that the higher inertia particles are more easily trapped in the stagnation zone of secondary flows with low turbulence intensity in the corner region. In the near-wall region, the heavier particles ($St^+ \geq 25$) are prone to reside and form elongated clusters along the low speed streamwise velocity streaks, with this trend less pronounced with increasing Stokes number. Along the wall, away from the corner where the secondary motion is attenuated, particle accumulation is dominated by the near-wall coherent vortices. This phenomenon is further discussed using a region-based correlation analysis between the particle spatial distribution and local flow topology. An in-depth particle dynamic analysis determines that the average cross-sectional drag force resulting from the secondary flow is mainly responsible for the

particle motion throughout the duct cross-section, which tends to push particles away from the walls in the near-wall region, but shows the exact opposite trend in the bulk flow region. Moreover, the pressure gradient force also plays an important role for low-inertia particles. As the Stokes number is increased, the lift force becomes progressively dominant in the viscous sublayer, acting to pull particles towards the corners and walls of the duct. Finally, the effect of two-way coupling on particle accumulation is briefly discussed although, due to the present low particle volume fraction, the effect is found to be relatively weak.

I. INTRODUCTION

The transport of inertial particles in turbulence is commonly encountered in many environmental processes and engineering applications. Sediment transport in rivers, pollutant dispersion, pneumatic conveying, chemical reactors, and nuclear waste slurries are all typical examples. It has been recognized that preferential concentration and clustering of inertial particles occur frequently in these particle-laden flows, which are mainly induced by the interactions between the particles and the local turbulence structures. In terms of the mechanisms underlying preferential concentration, the vortical centrifuging effect was the first to be accepted in homogeneous isotropic turbulence (HIT). According to this mechanism, particles tend to accumulate in regions of low vorticity and high strain rate[1] and the accumulation level is significantly modulated by the particle Stokes number, with the largest preferential collections found when the particle Stokes number (based on the fluid Kolmogorov time scale) equals unity[2,3]. Vassilicos and co-workers[4,5] pointed out that the centrifuging effect is not applicable to the clustering of high-inertia particles, and proposed an alternative "sweep-stick" mechanism in HIT, which indicates that heavy particles preferentially stick to the zero-acceleration point of the turbulent flow, with small-scale clustering swept by the large-scale structures. Their theory was later verified in the experimental investigations of Obligado et al[6]. As for wall-bounded turbulence with one anisotropic direction (channels, circular pipes, boundary layers), the effects of turbophoresis[7,8] are known to be responsible for particle wall accumulation. The particle transfer process was also found to be significantly correlated with the near-wall coherent structures, a fact corroborated by Rouson and Eaton[9], Marchioli and Soldati[10,11] and Mortimer et al[12] through analysis of the relationship between the particle distribution and flow topology. These near-wall structures generally include sweeps, ejections events and quasi-streamwise vortices and, under the impacts of them, inertial particles are prone to migrate into low-speed fluid regions and form streamwise-elongated streaks[8-13]. Sardina et al[14] reported that both small-scale clustering and turbophoresis can simultaneously exist in turbulent channel flows, and that the near-wall concentration is actually a consequence of the delicate balance between particles moving away from the wall due to the coherent structures and the opposite particle flux toward the wall induced by turbophoretic drift. In contrast, for more complex wall-bounded cases with two anisotropic directions, such as turbulent square duct flows, in addition to the aforementioned turbulent structures, the presence of cross-sectional turbulence-driven secondary motions[15-17] adds

an extra effect on the dispersive behaviour of particles embedded within the flow. Presently, there is not a complete understanding of the fundamental mechanisms responsible for the preferential concentration of inertial particles in turbulent square duct flows due to the limited studies performed to date. Accordingly, the focus of the present study is on elucidating the dynamics surrounding the preferential accumulation of particles induced by secondary flows in the square duct.

Many of the previous investigations on particle-laden flows in square ducts were conducted by point-particle simulations. Winkler et al[18] first simulated the preferential concentration in a vertical square duct flow using large eddy simulation one-way coupled with Lagrangian particle tracking (LPT) at $Re_\tau = 180$ (based on the duct half-width h and the mean friction velocity u_τ). They found that particles tend to accumulate in regions of high strain-rate and low swirl strength, with the most pronounced concentration in the near-wall and vortex regions of the duct cross-section. Sharma and Phares[19] further studied particle transport in a horizontal square duct without consideration of the gravitational force at $Re_\tau = 150$, and the secondary flows were shown to enhance the lateral mixing of low-inertia particles, whereas high-inertia particles had a tendency to spread out more efficiently near the low-speed streaks of near-wall regions in the streamwise direction. Particle dispersion in a turbulent square duct flow with a much higher $Re_\tau = 5275$ was investigated by Fairweather and Yao[20], where they proposed that the secondary flow could result in the uniform distribution of small particles and encourage large particles to concentrate at the duct corners. Gravity was also found to play an important role in the accumulation of the large particles in their work. Furthermore, particle deposition in the same geometry was also analyzed by these authors[21-23], and it was demonstrated that the off-axis secondary flow could cause high-inertia particles to preferentially deposit in duct corners and low-inertia particles in the central regions of the duct walls. More recently, Noorani et al[24] studied the effect of duct aspect ratio on particle behaviour, concluding that the secondary flow topology in a square duct significantly differs from that in rectangular duct. Due to this difference, the largest particle concentration in the viscous sublayer appears at the symmetry plane of a square duct, whereas the accumulation peak in a rectangular duct occurs at a position having a finite distance from the central plane. In addition, the particle turbulence kinetic energy, velocity fluctuations and accelerations were all observed to be sensitive to the particle inertia.

As well as the above-mentioned point-particle based studies, which are generally used to deal

with particle-laden flows with particle sizes smaller than the Kolmogorov length scale and low particle volume fraction ($\emptyset \leq 10^{-3}$), particle-resolved direct numerical simulations (DNS) have also been adopted in recent years to investigate the interaction mechanisms between the different phases in particle-laden flows. This simulation method requires the flow structures around a particle to be fully resolved, so that the particle size needs to be relatively large in comparison with the smallest turbulence scales, which thus limits the particle number that can be used. There are two research groups that have used this method to study particle-laden flows in a square duct. Lin et al[25] performed DNS with a direct-forcing fictitious domain method to consider the effect of finite-sized neutrally buoyant particles on the turbulence in a square duct with a relatively high particle volume fraction ($\emptyset = 0.008 - 0.07$), with their results showing that particles preferentially concentrate in the duct corner regions, and that the presence of particles enhances the mean secondary flow, with its vortex centre shifting closer to the duct core regions. Fornari et al[26] also discussed turbulence modulation by such particles using DNS combined with an immersed boundary method but considered a wider range of particle volume fractions ($\emptyset = 0.0 - 0.2$). It was found that there exists a critical point for the particle volume fraction ($\emptyset = 0.1$) where the intensity of the secondary flow was observed to be enhanced and particles were prone to accumulate in the duct corners when $\emptyset \leq 0.1$, whilst above this value the turbulence and secondary motions were reduced in strength, with particles preferentially concentrated in the duct core region. Additionally, Zade et al.[27] conducted experiments of turbulent flow with buoyant particles in a square duct, with their simulation results well verified by experimental observations.

Most previous investigations have focused on particle-laden flows with a fixed particle-to-fluid density ratio, the variation of which has been demonstrated to have a large effect on particle dispersion and dynamics[28]. Therefore, by conducting direct numerical simulation combined with Lagrangian particle tracking of one-way and two-way coupled flows, the present work aims to elucidate the mechanisms underlying particle preferential accumulation induced by the secondary flows in a dilute turbulent square duct at $Re_\tau = 300$, with a wide range of shear Stokes numbers considered ($St^+ = 0.31 - 260$) achieved by varying the particle-fluid density ratio ($\rho_p^* = 2.5 - 2076$) at a fixed particle size. The paper is organized as follows: the computational methodologies used for the fluid phase and particulate phase predictions are introduced in Section II. Validation of the single-phase flow predictions is given in Section III.A, and results for particle concentration,

spatial distribution, velocity statistics, correlation with flow topology and hydrodynamics are presented and analyzed in Section III.B, with the effects of two-way coupling on particle accumulation discussed in Section III.C. Finally, concluding remarks are summarized in Section IV.

II. METHODOLOGY

A. Flow configuration

A schematic of the geometry and coordinate system used for the present square duct flow is shown in Fig. 1. The computational domain size is $8\pi h \times 2h \times 2h$ in the (x, y, z) directions, and the coordinate origin is located at the duct centre, with *x* axis aligned with the streamwise direction, the *y* axis in the vertical direction and the *z* axis in the spanwise direction. The corresponding flow velocity components are $\vec{u} = (u, v, w)$, respectively. The length of the domain was chosen to be long enough to accommodate the largest turbulent structures in the streamwise direction at the present Reynolds number[29,30], and the same length was also adopted by Yao and Fairweather[23] and Noorani et al[24] in their studies of duct flows. No-slip boundaries were imposed on the four walls, with periodic boundary conditions applied at the inlet and outlet of the duct.

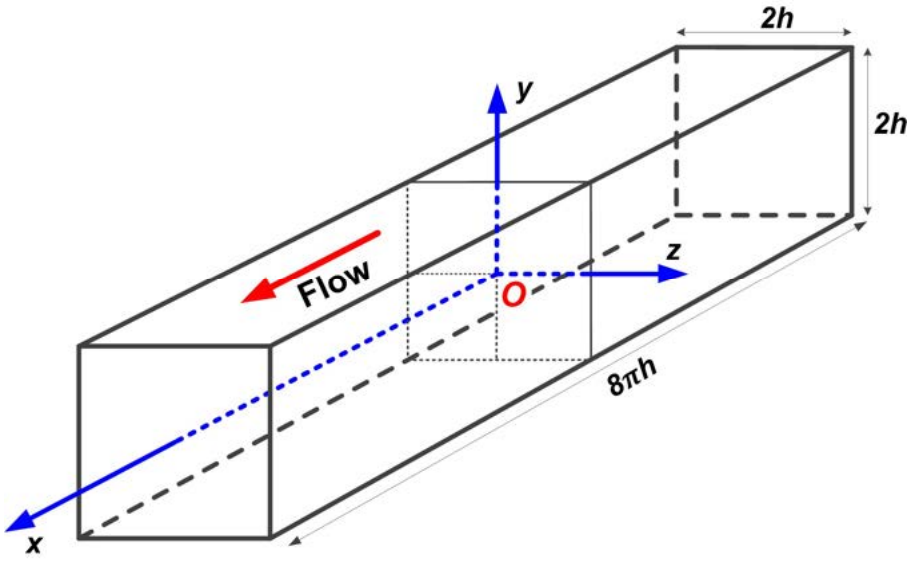

FIG. 1. Coordinate system and geometry of the square duct.

The bulk Reynolds number for the present flow was 4890, which is defined as $Re_b = u_b h/\nu$, where ν is the kinetic viscosity and u_b the bulk velocity, and the corresponding shear Reynolds

number was Re_τ =300. The mean friction velocity is defined as $u_\tau = \sqrt{\tau_w/\rho_f}$, where τ_w is the mean shear stress over the four duct walls and ρ_f is the fluid density. In the present work, the velocity, length and time scales are made dimensionless either using viscous scales ("+"), i.e. $u^+ = u/u_\tau$, $x^+ = (x+h)u_\tau/\nu$ and $t^+ = tu_\tau^2/\nu$, or using integral scales ("*"), i.e. $u^* = u/u_b$, $x^* = x/h$ and $t^* = tu_b/h$.

B. Direct numerical simulation

Direct numerical simulations with the code Nek5000[31] were conducted to model the present incompressible Newtonian flows in the square duct. This code is based on the spectral-element method, in which the computational domain is divided into hexahedral local elements and the solution is given at the Gauss–Lobatto–Legendre quadrature points using Lagrange polynomials of order *N* within each element. Due to its high-order accuracy and efficient parallelization capabilities, this code has been widely accepted and validated in many DNS applications to wall-bounded flows[12,16,24,32], which is why it is adopted for the present work. A continuous phase discretization using 48 × 24 × 24 8th order elements (i.e. 9.6M nodes) was applied to the present computational domain, with the spectral elements distributed uniformly in the *x* direction and clustered towards the walls in the *y* and z directions. A fixed maximum fluid solver time step was used ($\Delta t^* = 0.002$), with the corresponding Courant–Friedrichs–Lewy number always less than 0.5. Additionally, a dynamic pressure gradient was employed in the streamwise direction to maintain a constant mass flow rate. The Navier-Stokes equations, non-dimensionalized by using the duct half-width h, the bulk velocity u_b and the fluid density ρ_f, are given as follows:

$$\nabla \cdot \vec{u}^* = 0 \tag{1}$$

$$\frac{\partial \vec{u}^*}{\partial t^*} + \vec{u}^* \cdot \nabla \vec{u}^* = -\nabla p^* + \frac{1}{Re_b} \nabla \cdot \tau^* + \vec{f}^* + \vec{f}_p^* \tag{2}$$

where $\vec{u}^*$ is the fluid velocity, p^* is the fluid pressure, τ^* is the viscous stress tensor, $\vec{f}^*$ is an extra source term used to maintain a constant mass flow rate, and $\vec{f}_p^*$ is the force acting on the local fluid exerted by the surrounding particles, which is employed when two-way coupling is considered. More details about the spectral element method and the code can be found elsewhere[16,24,31].

C. Lagrangian particle tracking

In the present work, particle motion was described by a Lagrangian particle tracking

technique[12], in which particles are tracked within the fully developed turbulent flow domain along their calculated trajectories. This point-source method is acceptable since the particle size was lower than the smallest Kolmogorov scale present within the turbulent flow. Particle motion in turbulent flows are generally governed by the drag force, lift force, virtual mass force, pressure gradient force, Basset history force, and gravity/buoyancy[33]. According to Armenio and Fiorotto[34], the pressure gradient force only becomes relevant when the particle-to-fluid density is of $O(1)$. Due to the wide range of particle-to-fluid density ratios ($\rho_p^* = 2.5{\sim}2076$) considered herein, used to study the sensitivity of the secondary flows to particle inertia, the pressure gradient force must be accounted for. In contrast, the Basset history force was not considered due to the requirement of long computation times, but also since its contribution is much smaller than that of the drag force when the particle size $d^+ \leq O(1)$[35,36]. Gravity and buoyancy were also ignored in order to isolate the effect of the secondary flows on particle behaviour. Furthermore, the lift force resulting from self-induced particle rotation is much less important than that of the shear-induced component and thus was also neglected[37]. Since the present particle-laden flows were relatively dilute with particle volume fractions $\emptyset \leq 10^{-4}$, inter-particle collisions we not accounted for. All particles were represented by rigid spheres with the same diameter, and particle-wall collisions were considered to be fully elastic. Hence, based on the above simplifications and to interface with Nek5000, the particle motion equation, non-dimensionalized in the same manner as the fluid phase, can be given in the following form:

$$\frac{d\vec{u}_p^*}{dt^*} = \frac{3C_D|\vec{u}_s^*|}{4d_p^*\rho_p^*}\vec{u}_s^* + \frac{3C_L}{4\rho_p^*}(\vec{u}_s^* \times \vec{\omega}^*) + \frac{C_{am}}{\rho_p^*}\left(\frac{D\vec{u}^*}{Dt^*} - \frac{d\vec{u}_p^*}{dt^*}\right) + \frac{1}{\rho_p^*}\frac{D\vec{u}^*}{Dt^*} \tag{3}$$

where the terms on the right hand side of Eq. (3), in order, represent the drag, shear-induced lift, virtual mass and pressure gradient forces. $\vec{u}_p^*$ is the particle velocity, $\vec{u}_s^* = \vec{u}^* - \vec{u}_p^*$ is the relative slip velocity, d_p^* is the particle diameter, the particle-to-fluid density ratio is defined as $\rho_p^* = \rho_p/\rho_f$, ρ_p is the particle density, $\vec{\omega}^* = \nabla \times \vec{u}^*$ is the local flow vorticity at the particle location, and $D\vec{u}^*/Dt^*$ is the total fluid acceleration evaluated instantaneously at the particle location by the high accuracy spectral interpolation algorithm in Nek5000. C_{am} is the added mass force coefficient, and its value is 0.5 for spherical particles[38]. C_D and C_L are the Stokes drag coefficient and slip-shear lift coefficient, respectively. Jin et al[39] found that the effect of near-wall corrections to the drag force on particle transport is significant when the shear particle Stokes number $St^+ >$

20, so the corrected C_D values from Zeng et al [37], where corrections for the wall-effect were made based on the experiments of Schiller and Naumann[40], were accepted in this work according to:

$$\begin{cases} C_D = \left(1 + 0.15\left(1 - e^{-\sqrt{\delta}}\right) Re_p{}^{0.687+0.313e^{-2\sqrt{\delta}}}\right) C_{D0}, & Re_p < 1000 \\ C_D = 0.44, & Re_p \geq 1000 \end{cases} \quad (4)$$

where

$$C_{D0} = \left(1.028 - \frac{0.07}{1+4\delta^2} - \frac{8}{15} ln\left(\frac{270\delta}{135+256\delta}\right)\right)\frac{24}{Re_p} \quad (5)$$

$$\delta = \frac{L^*}{d_p^*} - 0.5 \quad (6)$$

In Eq. (5), Re_p is the particle Reynolds number and is given by $Re_p = Re_b d_p^* |\vec{u}_s^*|$. L is the distance from the particle centre to the nearby wall. Similarly, the corrected slip-shear lift coefficient C_L is given by[37]:

$$C_L = C_{ls} \exp(-0.5\delta(Re_G/250)^{4/3}) \times (exp\,(\alpha(Re_G)\delta^{\beta(Re_G)}) - \lambda(\delta, Re_G)) \quad (7)$$

$$\begin{cases} C_{ls} & = 3.663/(Re_G^2 + 0.1173)^{0.22} \\ \alpha(Re_G) & = -exp(-0.3 + 0.0025Re_G) \\ \beta(Re_G) & = 0.8 + 0.01Re_G \\ \lambda(\delta, Re_G) & = (1 - exp\,(-\delta))(Re_G/250)^{5/2} \end{cases} \quad (8)$$

where Re_G is the Reynolds number of the shear flow, $Re_G = Re_b {d_p^*}^2 |\vec{\omega}^*|$ (for $Re_G \leq 200$).

A fourth-order Runge–Kutta scheme was applied to integrate Eq. (3). Particles were initially distributed randomly throughout the duct, with an initial velocity set equal to the interpolated fluid velocity at the particle location. The particle solver integration time step was set to be the same as the flow time step, which was much smaller than the smallest particle relaxation time to ensure that particle trajectories were fully resolved. For particles that exited the duct in the streamwise direction, periodic boundaries were used to reintroduce them back into the computational domain at the corresponding location at the duct inlet. Four particle-to-fluid density ratios ranging between 2.5 and 2076 were considered in this study, which is analogous to the continuous phase varying from water to air, provided that the particle material is glass. For each particle set, the trajectories of 100,000 particles were calculated to ensure the independence of particle statistics on particle number (N_p). Although the present particle volume fraction over the whole domain was relatively low ($\emptyset \leq 10^{-4}$), the local particle concentration induced by the secondary flows or near-wall turbulent structures could be much larger and may affect the local flow significantly in the near-wall regions, which possibly in turn could generate a different particle distribution. To examine this, the effect of two-way coupling on each particle set was also studied. Here, the particles' effect on the local fluid

phase was taken into account by imposing an additional source term in the momentum equation, Eq. (2):

$$\vec{f}_p^* = -\frac{1}{V_c^*}\sum_{P=1}^{N_P} F_p^* \tag{9}$$

where V_c^* is the volume of a computational cell, N_P is the number of particles in one cell, and F_p^* is the resultant fluid force exerted on a particle which can be obtained from the particle motion equation, Eq. (3). The dimensionless particle relaxation times, which measure the importance of particle inertia, based on the viscous scale (shear Stokes number St^+) and integral scale (bulk Stokes number St_b) are given by:

$$St^+ = Re_\tau^2 \frac{{d_p^*}^2 \rho_p^*}{18} \tag{10}$$

$$St_b = Re_b \frac{{d_p^*}^2 \rho_p^*}{18} \tag{11}$$

More details about the simulation parameters used for the particle phase can be found in Table I.

TABLE I Simulation parameters for the particle phase.

Parameter	$St^+ \approx 0.31$	$St^+ \approx 25$	$St^+ \approx 125$	$St^+ \approx 260$
N_p	100,000	100,000	100,000	100,000
St_b	0.0170	1.3583	6.7917	14.0995
St^+	0.3125	25.0	125.0	259.5
ρ_p^*	2.5	200	1000	2076
$\emptyset$	10^{-4}	10^{-4}	10^{-4}	10^{-4}
d_p^*	0.005	0.005	0.005	0.005
d_p^+	1.5	1.5	1.5	1.5
Δt^*	0.002	0.002	0.002	0.002
Δt^+	0.0368	0.0368	0.0368	0.0368

III. RESULTS AND DISCUSSION

In this section, the simulation results for the single-phase flow and particulate phase are analyzed. A brief discussion of the fluid phase flow results is provided to describe the typical mean characteristics of turbulent square duct flows and to ensure the sufficiently accurate predictions of the flow field before the particles are introduced. Attention is then focused on the analysis of particle Eulerian statistics under one-way coupling, which is used to uncover the mechanisms of preferential concentration caused by the turbulence-driven secondary flows. Finally, the effect of two-way coupling is reported.

A. Fluid flow validation

For the fluid phase, a fully developed turbulent channel flow at the indicated Reynolds number was used to initialize the flow field used later for particle-laden flow predictions. By monitoring the mean streamwise velocity, the root mean square (*r.m.s.*) of velocity fluctuations and the shear stress along the wall bisector, the simulation was performed until a statistically steady state of these parameters had been achieved. Flow statistics were then collected over 1500 integral time units. For the mean flow statistics reported hereinafter, apart from time averaging, spatial averaging in the streamwise direction and over the four quadrants of the duct cross-section was also applied. Figure 2(a) shows the cross-sectional distribution of mean secondary flow velocity vectors, and streamwise velocity contours normalized by the bulk velocity, in the lower-left quarter of the duct, where it is observed that two counter-rotating secondary vortices symmetric about the corner bisector are predicted. These secondary flow vortices transfer momentum from the duct core regions to the corners, thereby resulting in a bulge in the streamwise velocity contours towards the corner. The corresponding contours of the magnitude of the secondary velocity ($\sqrt{V^{*2} + W^{*2}}$), which reflect the intensity of secondary motions, is displayed in Fig. 2(b), where the largest secondary velocity is found in the near-wall regions and along the corner bisector close to the corner. Furthermore, the turbulence kinetic energy k^* is given in Fig. 2(c), and its maximum is found, as expected, to be close to the walls located at $z^*(y^*) \approx -0.951$ ($z^+(y^+) \approx 15$). It may also be noted that there exists a local minimum in the turbulence kinetic energy along the corner bisector. All these results are qualitatively consistent with those of Noorani et al[24] for flow in a turbulent square duct.

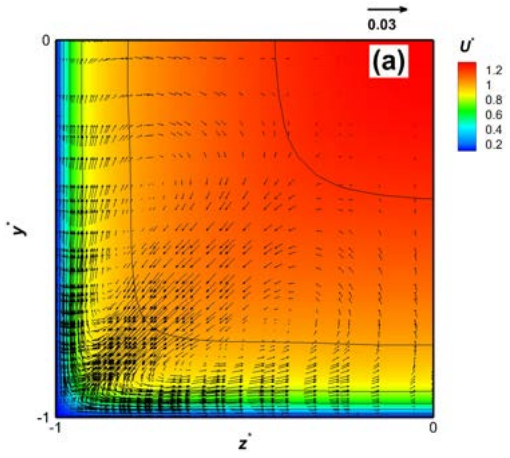

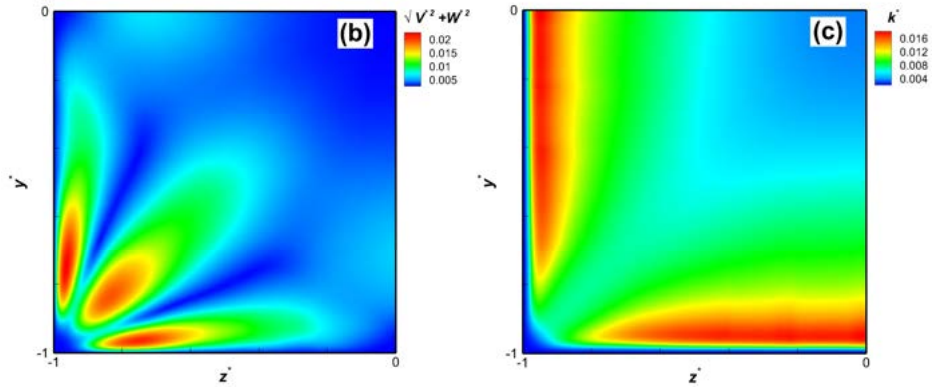

FIG. 2. Cross-sectional contours of average flow statistics normalized by bulk velocity u_b in one quarter of the square duct: (a) mean secondary flow vectors with the mean streamwise velocity superimposed, (b) magnitude of mean secondary velocity ($\sqrt{V^{*2}+W^{*2}}$), and (c) turbulence kinetic energy (k^*).

To further quantitively validate the accuracy of the flow field predictions, the mean flow statistical moments normalized by the local friction velocity (u_τ) are compared to the previous DNS results of Vinuesa et al[16] along the wall bisector in Fig. 3. The mean streamwise velocity and *r.m.s.* velocity fluctuations are in good agreement with the previous DNS results. However, for the Reynolds shear stress, the present DNS shows a slightly lower peak than previously obtained by Vinuesa et al[16], which is likely due to slight differences in the Reynolds numbers considered ($Re_\tau = 323$ in Vinuesa et al[16] compared to 300 in the present work) and numerical accuracy. Despite this, the excellent agreement generates confidence in the present predictions of the continuous phase flow field.

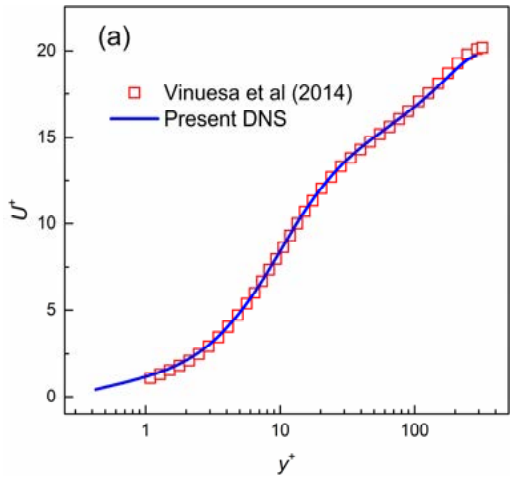

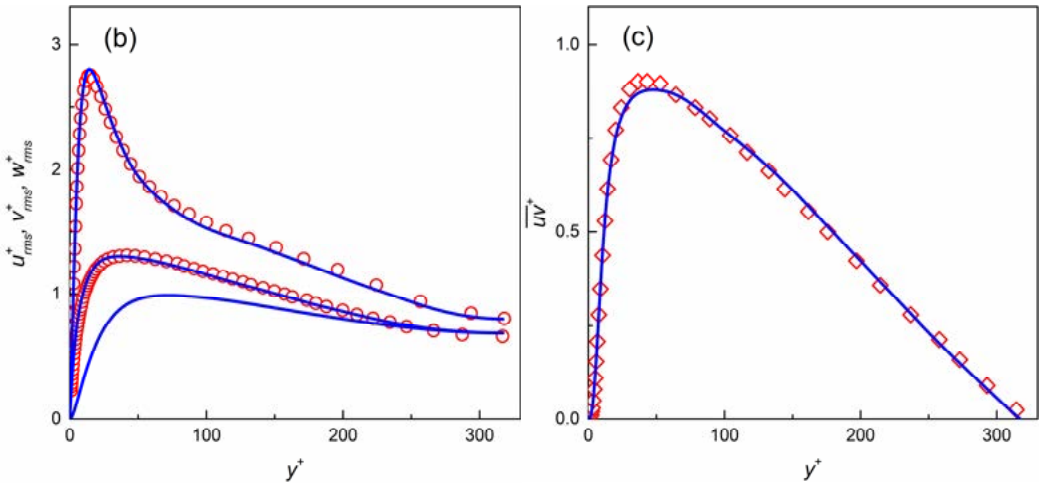

FIG. 3. Comparisons of average flow statistical moments normalized by local friction velocity (u_τ) with Vinuesa et al[16] along the wall bisector: (a) mean streamwise velocity, (b) root mean square (*r.m.s.*) of velocity fluctuations, and (c) Reynolds shear stress.

B. Particulate phase

After obtaining a reliable fully developed turbulent flow field, particles were injected into the flow. In order to calculate the mean Eulerian statistics of the Lagrangian particles, a non-uniform two-dimensional mesh was applied to the duct cross-section, with a total of 14,400 grid cells used for the representation of particle statistics. Similar to the flow statistics analysis, averages across time, the streamwise direction and over the four quadrants of the duct were also used for the particulate phase.

The instantaneous particle concentration C_{wall} in the near-wall region ($y^*(z^*) < -0.9$ or $y^+(z^+) < 30$), which is defined as the particle number divided by the volume of the enclosed region and normalized by the mean bulk particle concentration C_b in the whole domain, was used to monitor the particle dispersion statistics until they reached a dynamic statistically steady state. Figure 4 displays the temporal evolution of C_{wall}/C_b for all the particle sets considered, where the near-wall particle concentration gradually becomes stable when $t^* \geq 500$, with particle statistics starting to be gathered from this time. It is also apparent from Fig. 4 that the strongest particle accumulation in the near-wall region occurs for $St^+ = 25$ particles, which is in agreement with findings of Sardina et al[41] in turbulent boundary layers and Noorani et al[24] in duct flows. As is known[24,38], this is due to the fact that the effects of turbophoresis are a maximum at around this

Stokes number. Furthermore, the accumulation of such particles is also significantly affected by the secondary motions in the square duct, which will be elaborated upon later.

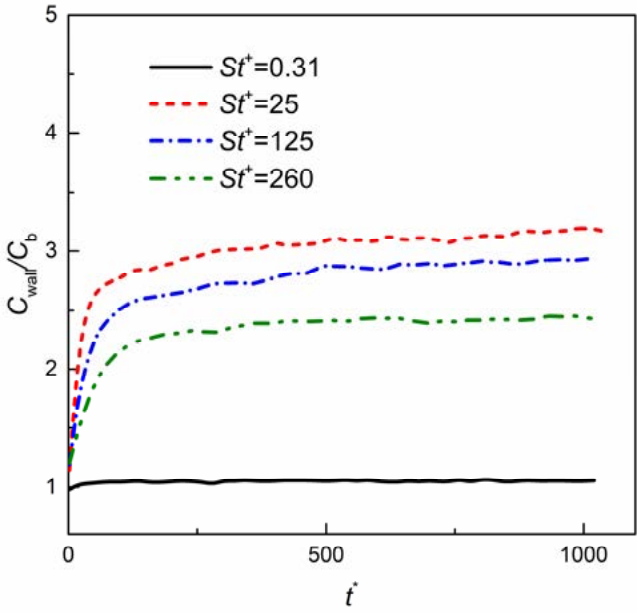

FIG. 4. Temporal evolution of the instantaneous near-wall particle concentration C_{wall} $(y^+(z^+) < 30)$ normalized by the mean bulk particle concentration C_b in the whole domain for all particle Stokes numbers considered.

1. Particle concentration and spatial distribution

To visualize the particle distribution in the duct cross-section, logarithmic two-dimensional contours of the mean particle concentration C normalized by the bulk concentration C_b for all the investigated particles were calculated and are presented in Fig. 5(a). Due to their low inertia, particles with $St^+ = 0.31$ follow the local flow closely and distribute relatively uniformly over the duct cross-section. The heavier particles ($St^+ \geq 25$), as anticipated, accumulate preferentially near the duct walls, with the highest levels of accumulation occurring in the duct corners. Furthermore, the concentration contours of these particles are observed to slightly deform towards the corner, which is caused by the cross-sectional secondary motions tending to drive particles firstly towards the corners and then moving them away along the walls to their central regions. However, because of their inertia, not all particles leave the corner region. Instead, they can be trapped there for long periods of time once captured[25,26], and the fundamental mechanism responsible for this behaviour

will be discussed in detail later. To quantify the sensitivity of particle accumulation to particle inertia, profiles of the mean normalized particle concentration along the wall bisector ($z^* = 0$) and in near-wall region ($z^* = -0.96$ or $z^+ = 10$) for different Stokes numbers are provided in Fig. 5(b) and Fig. 5(c). Along the wall bisector shown in Fig. 5(b), the concentration profiles are confirmed to exhibit a strong dependence on particle inertia, and this trend is similar that observed in canonical channel flows[12,14]. A concentration peak near the wall centre is evident for all particle sets, as expected, with the peak first increasing then decreasing in magnitude with the Stokes number, and with the most pronounced accumulation occurring for $St^+ = 25$ particles. This Stokes number is (when based on the characteristic time scale in the buffer layer) of order unity[14]. Since the total particle volume fraction in the domain is fixed, the transport of particles to the wall decreases the particle concentration outside the wall regions which gradually decline, hence the trend in particle concentration versus Stokes number in the outer regions is opposite to that in the near-wall region. In contrast, the profiles of particle concentration in the buffer layer ($z^+ = 10$) along the wall given in Fig. 5(c) are significantly different. Moving from the duct corner to the wall centre, the particle concentration is seen to first decrease then increase, and then become stable for particles with $St^+ \geq 25$. The reduction of particle concentration in the region $-0.95 < y^*(z^*) < -0.5$ can be explained by the effect of the near-wall secondary flows. As mentioned in relation to Fig. 2(b), the intensity of the secondary flow adjacent to the wall and close to the duct corners is relatively strong, and this is sufficient to push particles away from this region towards the central area of the duct walls. Beyond $y^* = -0.5$, the intensity of the secondary flows is attenuated and the particle concentration reaches a plateau in the middle regions of the duct walls ($-0.5 < y^*(z^*) < 0$). The particle spatial distribution in this region is hence mainly dependent on the dynamics of the near-wall coherent structures, as previously mentioned. Note that close to the corner inside the viscous sublayer, the dependence of particle concentration on Stokes number is consistent with that in the wall-centre region.

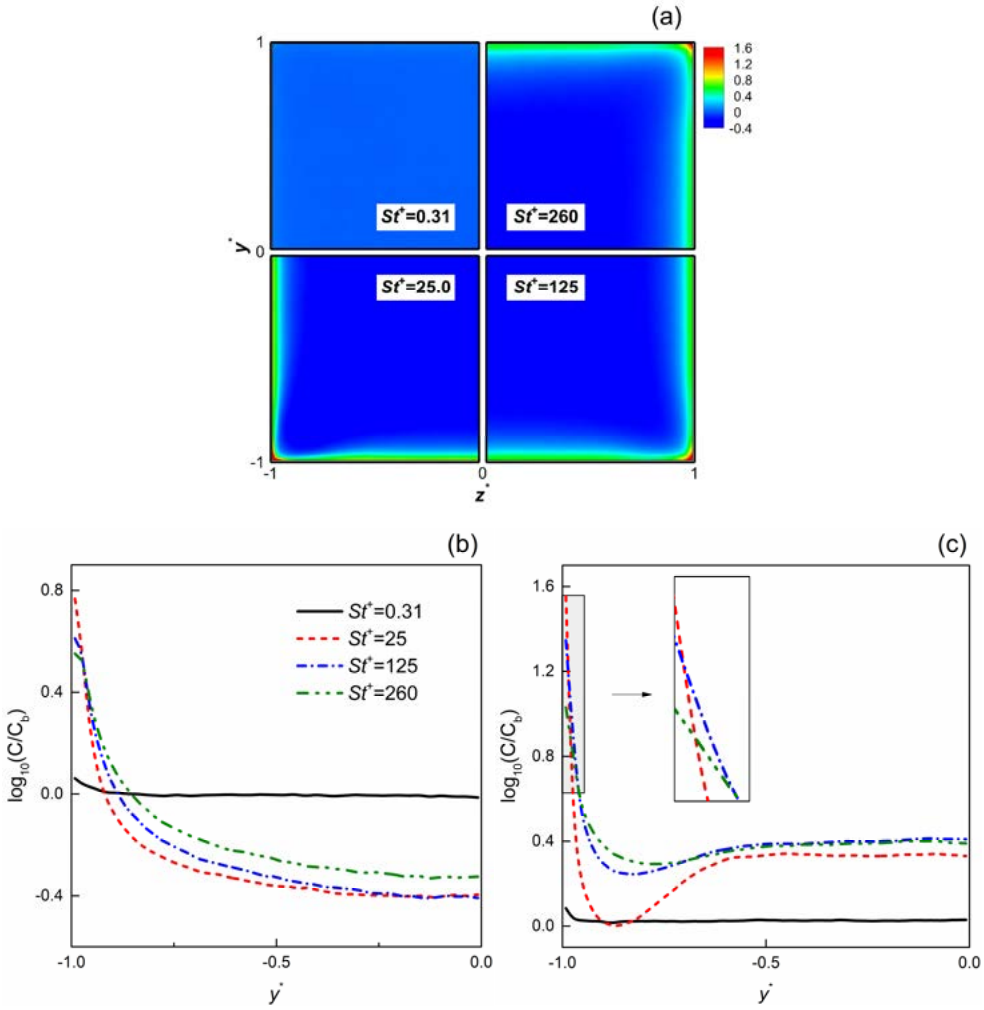

FIG. 5. Average normalized particle concentration in the duct cross section for the different particle Stokes numbers: (a) contours of the mean particle concentration (logarithmic value $log_{10}(C/C_b)$), and its profiles (b) at $z^* = 0$ along wall bisector and (c) at $z^*(z^+) = -0.96(10)$ in near-wall region.

Having observed that inertial particles accumulate near the duct walls, the instantaneous particle position and velocity in the near-wall regions are further analyzed to investigate the specific spatial patterns of the particle clustering. The Voronoi tessellation, first introduced to evaluate preferential concentration in turbulence by Monchaux et al[42] which has been widely used in wall-bounded turbulence[43,44], is adopted in the present study to measure the amount of particle clustering and the shape of particle clusters. Figure 6(a) presents a sample of an instantaneous realization for the $St^+ = 25$ particles in the near-wall region ($y^+ < 30$), with each particle surrounded by one individual Voronoi cell. At the spanwise wall boundaries, mirrored ghost-particles were applied to

close the open Voronoi cells[43]. According to the definition of the Voronoi diagram, the area of a Voronoi cell is negatively correlated to the local particle concentration, which means that small cell areas correspond to particle clusters with a high local concentration while large cell areas represent particle voids with low concentration. To distinguish the clusters from the particle distribution, the probability density function (PDF) of the Voronoi cell area A_v (normalized by the mean value $\bar{A}_v$) for all the considered particles is compared to the distribution of a random Poisson process[45] (RPP) in Fig. 7(a). It is clear that the PDFs of inertial particles deviate from the RPP, and particles form clusters (hereinafter referred to as a cluster region) when A_v is smaller than a threshold value A_v^*, with the corresponding PDFs found to be much higher than the RPP below that value. An exception to this is the lightest particle with $St^+ = 0.31$. Its PDF fits well with the RPP when $A_v > A_v^*$, although a few of these particles do form clusters in regions with $A_v < A_v^*$, probably due to the particle relaxation time which is close to that of certain small scale, near-wall coherent structures which can organize particles by their vortical centrifuging effect. For particles with $St^+ \geq 25$, the PDFs in the clustering region are observed to decline with increasing Stokes number, which implies that the level of clustering of these particles gradually weakens with increasing particle inertia. Note that the PDF values for the $St^+ = 25$ particles in the cluster region are the largest, suggesting that these particles have the greatest extent of accumulation. The cluster regions are highlighted in Fig. 6(b) which corresponds to Fig. 6(a). These particle clusters tend to form in streamwise-elongated streaky structures both in the duct corners and the central regions of the duct walls. Particles from these clusters are transported towards the wall mainly by the strong coherent ejections and sweeps in these regions, which resemble those in turbulent wall boundary layers[11]. However, differences occur due to the restriction of the sidewalls and the sweeping of the instantaneous secondary flows, so that the distribution of these clustered particle streaks along the duct walls in the spanwise direction is more organized and regular than that in channel flows or wall boundary layers.

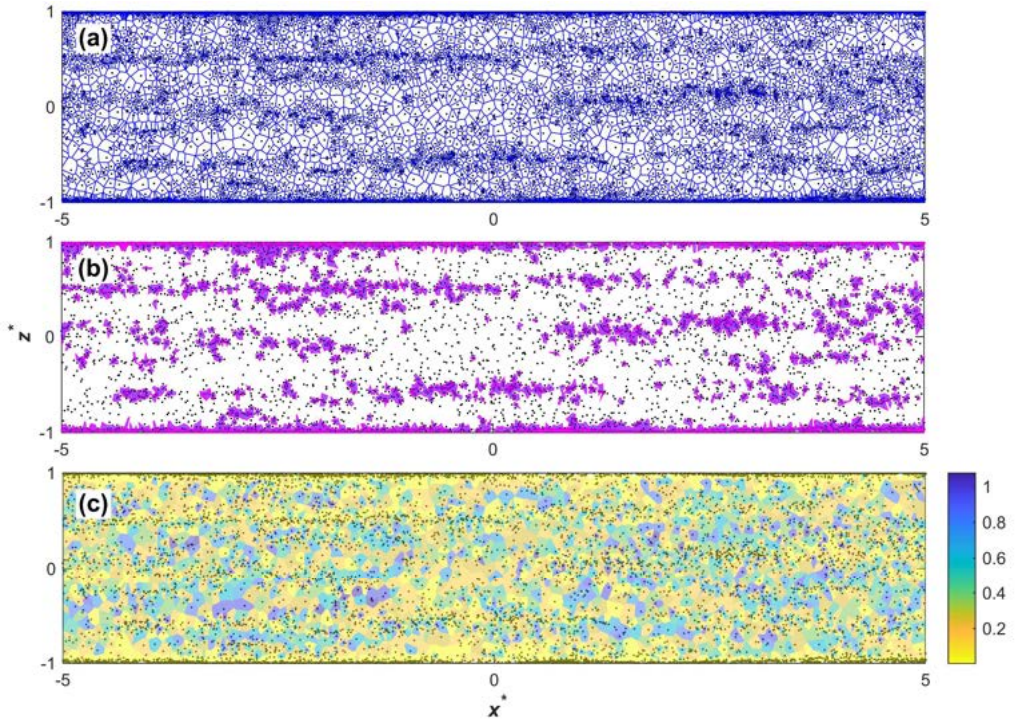

FIG. 6. Voronoi tessellation diagram for $St^+ = 25$ particles: (a) in a sample near-wall realization ($y^+ < 30$) with (b) highlighted clusters (marked in magenta) and (c) the Voronoi cell coloured by the streamwise particle velocity.

To quantitatively measure the anisotropy of the elongated particle clusters, the PDFs of the Voronoi cell aspect ratios $L_{v,x}/L_{v,z}$ (the ratio between the maximum length of the Voronoi cell $L_{v,x}$ in the streamwise direction and $L_{v,z}$ in the spanwise direction) for the different particle Stokes number particles in these regions are plotted in Fig. 7(b). An aspect ratio of $L_{v,x}/L_{v,z} \leq 1$ denotes that particle clusters are more likely to be aligned in streaks in the streamwise direction than in the spanwise direction. Obviously, the cumulative probability of $L_{v,x}/L_{v,z} \leq 1$ (the area enclosed by the PDF curve and the abscissa) is larger than that of $L_{v,x}/L_{v,z} > 1$ for all particle cases, which demonstrates that particles are prone to form streamwise-aligned streaky structures as noted visually in Fig. 6(a-b), with this trend weakened with increasing Stokes number when $St^+ \geq 25$. To further determine where these streamwise-aligned particle streaks concentrate, Fig. 7(c) displays the PDFs of the normalized in-cluster and global streamwise velocities for particles with $St^+ = 25 - 260$. It is apparent that the probability of the cluster velocity is much higher than the global velocity in the low-speed regions for all the particles considered, indicating that particle clusters are easily formed

in these regions. This corroborates the visual observations in Fig. 6(c), which shows the instantaneous particle distribution with its corresponding Voronoi cell coloured by the streamwise velocity for particles with $St^+ = 25$. Furthermore, it is interesting to note from Fig. 7(c) that the particle velocity decreases with increasing Stokes number in the low-speed regions.

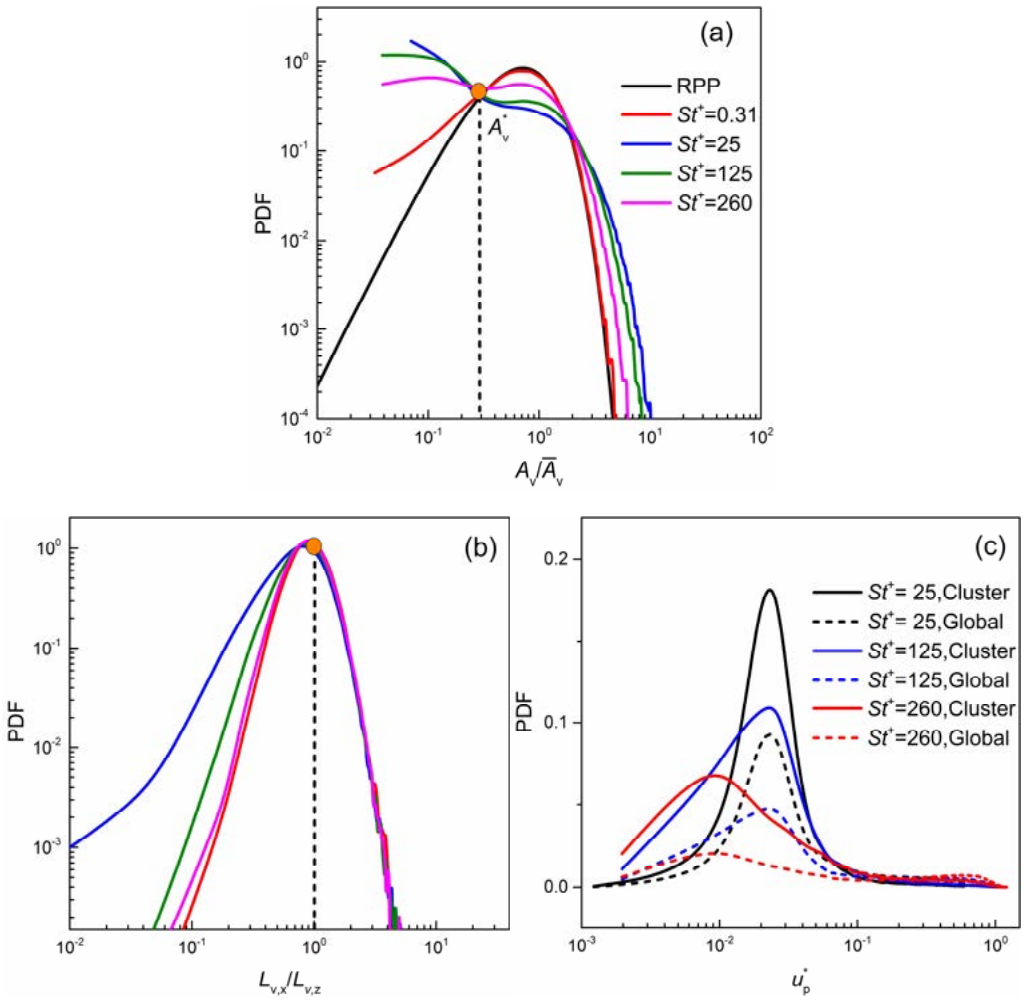

FIG. 7. PDFs of (a) the Voronoi cell area compared with a random Poisson distribution, (b) the Voronoi cell aspect ratio in the near-wall region ($y^+ < 30$), and (c) the normalized in-cluster and global velocities for particles with $St^+ \geq 25$.

2. Particle velocity statistics

In this sub-section the mean and fluctuating velocity statistics for the different Stokes number particles considered are reported, with the mechanisms underpinning particle accumulation in the

duct corners discussed. Figure 8(a) illustrates the distribution of the mean normalized streamwise particle velocity in the duct cross-section, with the contour plots shown in each quadrant in counterclockwise order for particles with $St^+ = 0.31 - 260$. These contours closely resemble those of the fluid phase in Fig.2(a), although the maximum streamwise particle velocity in the duct core regions is seen to decrease with increasing particle Stokes number. Comparisons of the mean streamwise velocity profiles for each particle set and the unladen flow along the wall bisector based on the integral and viscous scales are presented in Fig. 8(b) and Fig. 8(c), respectively. As anticipated, the lightest $St^+ = 0.31$ particles follow the flow due to their low inertia. With increases in Stokes number, the particles gradually lag behind the fluid phase in the outer region ($y^+ \geq 40$), which is due to the higher-inertia particles responding less rapidly to the local flow. In part of the buffer layer ($8 \leq y^+ \leq 20$), the velocity of the heavier particles ($St^+ \geq 25$) increases with Stokes number, but is still lower than the fluid phase, which can be explained by the canonical feature of particles preferentially accumulating in the low-speed regions of the wall-bounded turbulence. Conversely, the particle velocity is found to exceed that of the fluid in the very near-wall regions (viscous sublayer and part of the buffer layer), as can be seen clearly in Fig. 8(c), which is likely due to effect of the near-wall coherent sweep events driving particles with high streamwise momentum from the outer layer towards the wall regions. These phenomena in the square duct are consistent with previous numerical and experimental studies of channel flows[12,46,47].

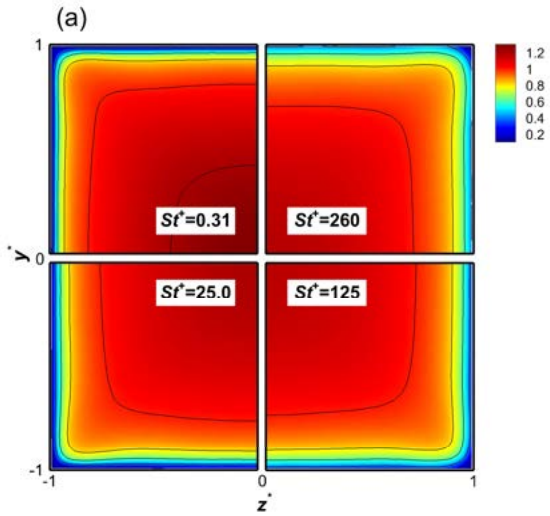

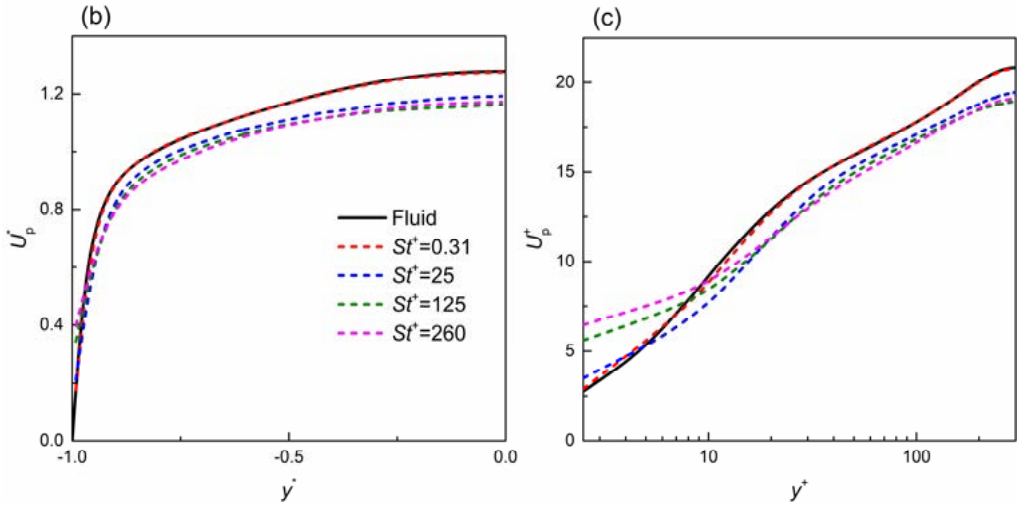

FIG. 8. Mean streamwise velocity for the different particle Stokes numbers: (a) contours of the mean streamwise particle velocity (U_p^*), and its profiles compared with the mean streamwise fluid velocity along the wall bisector based on (b) the integral scale and (c) the viscous scale.

The distribution of the mean secondary flow velocity ($\sqrt{V_p^{*2} + W_p^{*2}}$) over the duct cross-section for all indicated particles is shown in Fig.9(a). The basic topology of the mean secondary flow vectors for the solid particle phase is again similar to that of the fluid phase. However, the magnitude of the mean secondary particle velocity is observed to be significantly dependent on the particle Stokes number, especially along the duct diagonal and in the near-wall region near the corners, where local maxima in the particle velocity are found. More details can be extracted from Figs. 9(b, c), which show comparisons of the secondary flow velocity for the two phases at $z^* = y^*$ along the corner bisector and at $z^*(z^+) = -0.96(10)$ in the near-wall region. In Fig. 9(b), as the distance away from the corner along the corner bisector increases, the magnitude of the mean secondary particle velocity first increases then decreases, with the location of its maximum located at approximately $y^* = -0.84$. A similar trend is observed for all Stokes number particles, with the maximum peak value found for $St^+ = 25$, in agreement with previous findings[24]. Again, it is worth noting that the bulk Stokes number based on the integral scale of the flow for $St^+ = 25$ particles is close to unity. Furthermore, the greater the intensity of the secondary particle velocity, the closer the location of its peak is to the duct corner. In contrast, the distribution of the secondary particle velocity adjacent to the wall at $z^+ = 10$ shown in Fig. 9(c) is significantly different. In the region of $y^* \leq -0.2$, the intensity of the wall-parallel secondary particle motion largely decreases with

increasing Stokes number, and a local maximum is found in this region for all given particles, with the location of this peak varying with particle inertia. Also, in the region close to the corner ($y^* < -0.7$), another local maximum is observed for the $St^+ = 25,125$ particles, which occurs since this position coincides with the corner bisector region, where the secondary motions impact strongly on the particle phase, as already noted.

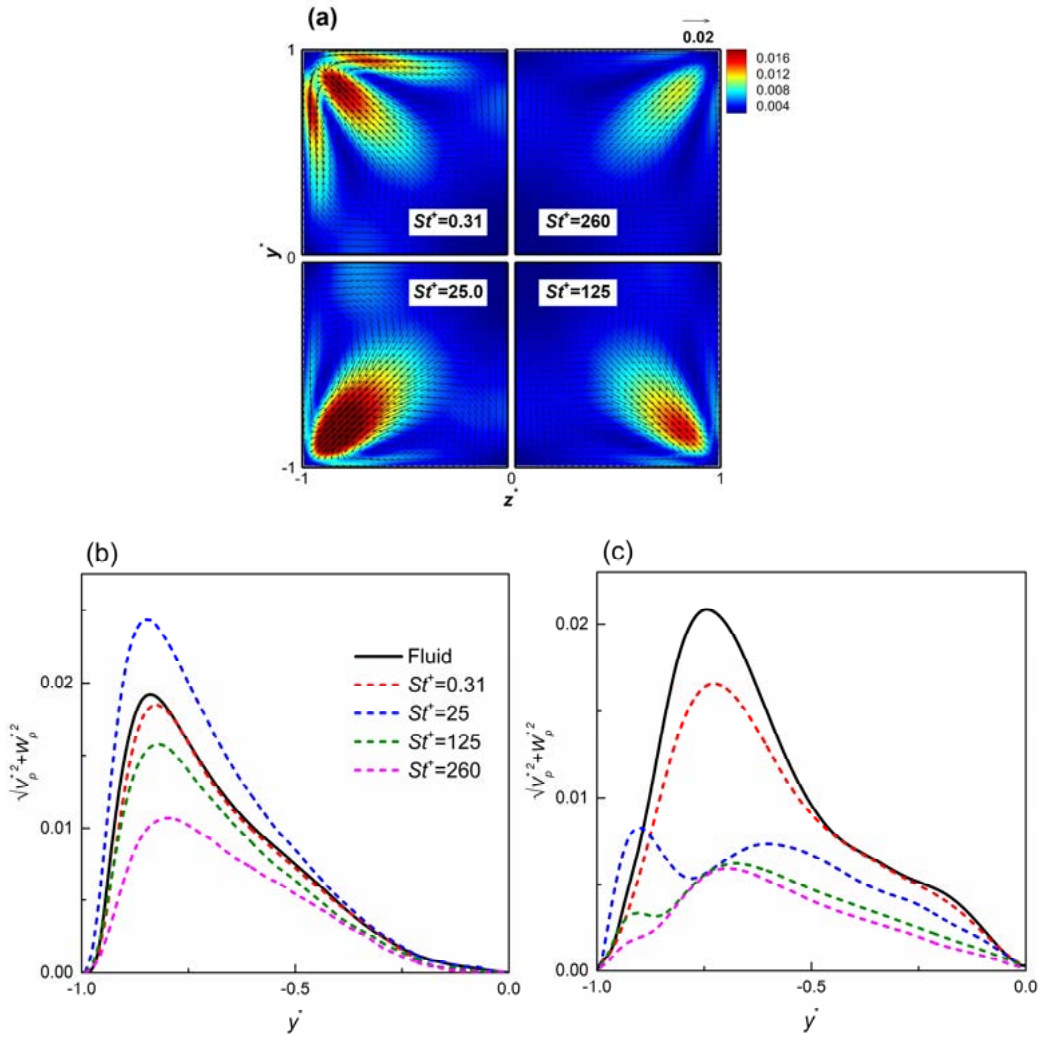

FIG. 9. Time and space-averaged secondary flow velocity of the given particles: (a) contours and vector fields of the secondary flow velocity $\sqrt{V_p^{*2} + W_p^{*2}}$, and its profiles compared with the flow secondary velocity (b) at $z^* = y^*$ along the corner bisector and (c) at $z^*(z^+) = -0.96(10)$ in the near-wall region.

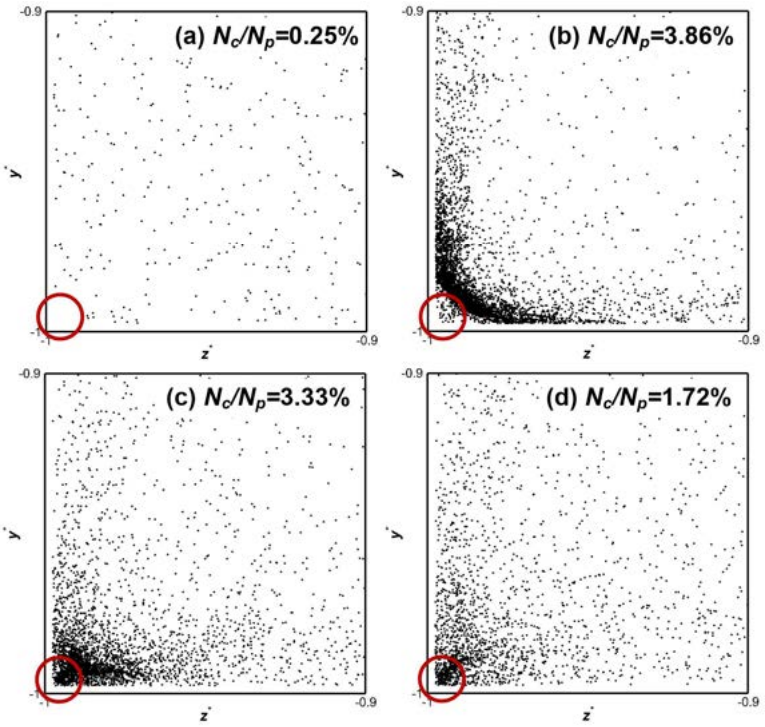

FIG.10. Instantaneous particle distribution in the duct corner regions ($z^*(z^+) < -0.9(30), y^*(y^+) < -0.9(30)$) for different Stokes number particles: (a) $St^+ = 0.31$, (b) $St^+ = 25$, (c) $St^+ = 125$, and (d) $St^+ = 260$.

As expected, the particle distribution in the duct cross-section is controlled by the secondary particle velocity. Figure 10 depicts the instantaneous distribution of particles with different Stokes numbers in the region near the corner ($z^*(z^+) < -0.9(30), y^*(y^+) < -0.9(30)$) at the final timestep of the simulation. We observe that the $St^+ = 0.31$ particles are randomly distributed, while the particles with $St^+ \geq 25$ accumulate largely in the corner region, with the ratio of the particle number (N_c) to the total particle number (N_p) in the corner region, expressed as a percentage, being 3.86% for the $St^+ = 25$, 3.33% for the $St^+ = 125$ and 1.72% for the $St^+ = 260$ particles, confirming the observations made in relation to Fig. 5. In addition to the different clustering levels, the accumulation pattern is also substantially dependent on particle inertia. For the low-inertia $St^+ = 0.31$ particles, these follow the secondary flow motion closely and none enter the stagnation region (highlighted with a red circle) of the secondary flow in the corner. For the mid-inertia $St^+ = 25$ particles, only a small fraction of them concentrate in the stagnation area, with most of them concentrating and extending along the walls close to the corner by following the

streamlines of the mean secondary motion adjacent to the walls. For the most inertial particles with $St^+ = 125, 260$, the particles concentrate mostly within the stagnation region and their accumulation patterns are distinct from that of the $St^+ = 25$ particles. This can be understood by considering that the secondary flow velocities after the turning point (the point near the corner where the direction of the secondary flow turns approximately 45°) are not sufficiently strong to continue to support the particles in following the wall-parallel secondary motions away from the corner, with the magnitude of the secondary particle velocity adjacent to the walls being much lower than for the low-inertia particles, as observed in Fig. 9(c). However, the particles still retain the high-momentum obtained from the flow in the corner bisector region because of their high inertia and, as a result, they migrate into the stagnation area where they reside for a long time.

Figure 11 further presents comparisons between the profiles of fluid and particle velocity fluctuations (*r.m.s.* values) along the wall bisector ($z^* = 0$) and at $z^*(z^+) = -0.96(10)$ in the near-wall region. Along the wall bisector shown in Figs. 11(a-c), the particle streamwise-velocity fluctuations are greatly enhanced compared with the fluid phase, which is induced by the gradient in the mean flow velocity through the wall-normal movement of the particulate phase, with this effect more pronounced for high-inertia particles[48]. Inversely, the particle *r.m.s.* values in the vertical and spanwise directions are suppressed, with these *r.m.s.* profiles decreasing and gradually becoming flattened with increasing Stoke number, which has also been observed in canonical channel flows[12,48]. The exception is the $St^+ = 0.31$ particle whose *r.m.s.* values in the vertical and spanwise direction are larger than that of the fluid phase in most regions, with the mean wall-normal secondary flow towards the duct centre having a slight effect. Moreover, unlike the fluid, the particle *r.m.s.* values do not go to zero at the wall, which is due to the fact that the particle velocity was not subjected to no-slip wall boundaries. Similar trends in the variation of particle velocity fluctuations with Stokes number are shared by the *r.m.s.* profiles along the sidewall in the near-wall region in Fig. 11(d-e). By comparing Fig. 11(b) to Fig. 11(c), the *r.m.s.* velocities in the vertical wall-normal direction are smaller than those in the wall-parallel direction. Furthermore, from Fig. 11(e, f) the *r.m.s* values close to the corner in the near-wall region in both directions are found to be lower than in the wall central regions, indicating that the turbulence intensity in the near-corner region is very low. It is also interesting to note from Fig. 11(f) that the positions of the local maxima in w^+_{prms} vary with particle Stokes number, and the direction of the w^+_{prms} gradient acts in the opposite sense

to that of the mean particle concentration profiles in Fig.5(c), which is most likely related to the different wall-normal secondary particle velocity in this region.

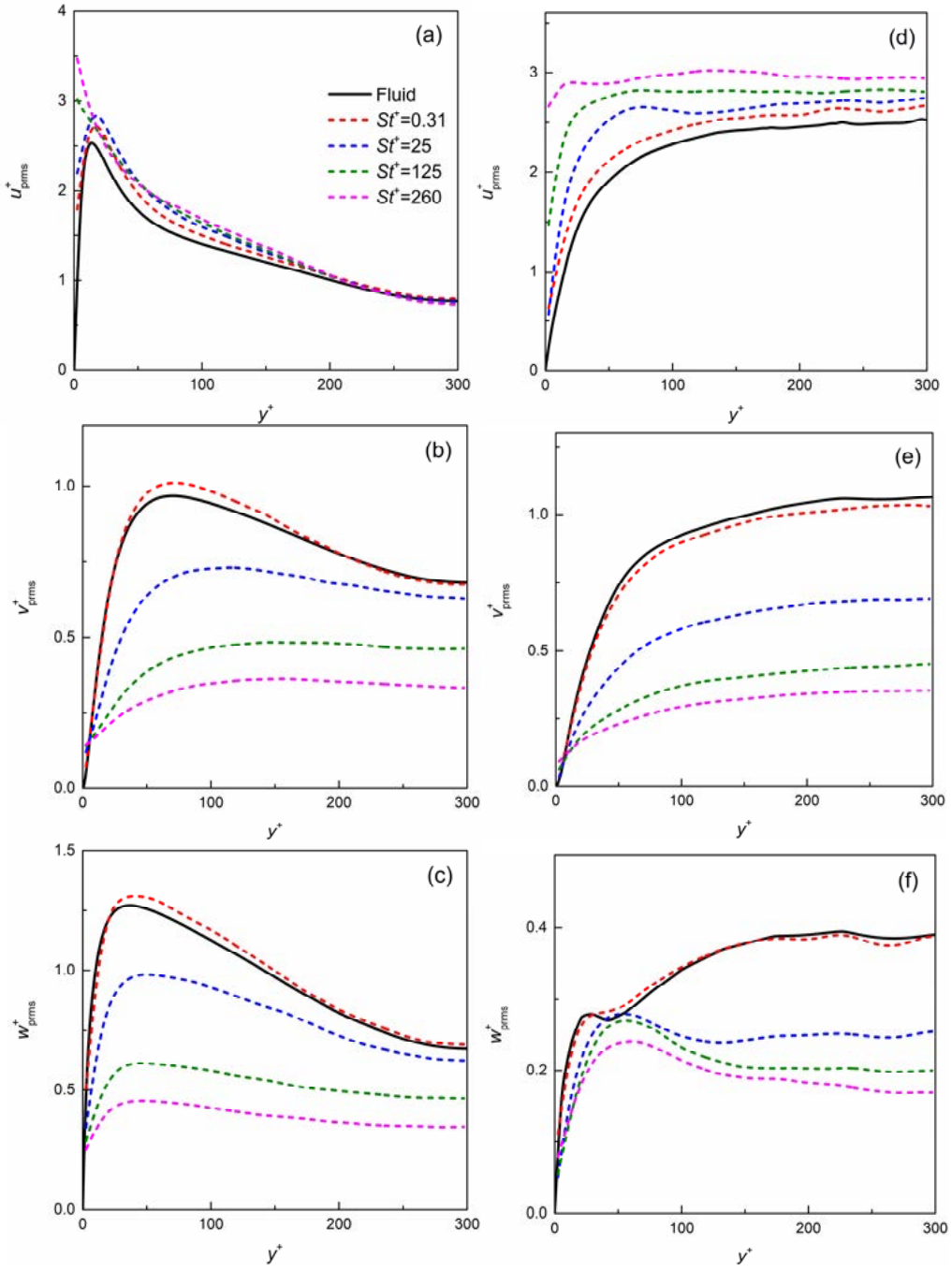

FIG. 11. Profiles of fluid and particle velocity fluctuations: (a, d) streamwise, (b, e) vertical and (c, f) spanwise components along (a, b, c) the wall bisector ($z^* = 0$) and (d, e, f) at $z^*(z^+) = -0.96(10)$ in the near-wall region.

Based on the above analysis, the mechanism for particle accumulation in the duct cross-section

is summarized in Fig. 12(a). The low-inertia particles ($St^+ = 0.31$) follow the secondary motion along the corner bisector moving from the duct core towards the corner, then turn approximately 45° and move along the wall to its centre area, finally returning back into the duct central regions along the wall bisector. However, heavier particles ($St^+ \geq 25$) cannot follow the flow and finish the whole cycle of the secondary motion, and most of them tend to accumulate in the corner region under the action of the strong secondary flow (region "A" marked in yellow) along the corner bisector. Among them, the mid-inertia particles ($St^+ = 25$) can still follow the streamlines of the wall-parallel secondary flow along the wall for a short distance and hence tend to be clustered along the trajectory of the wall-parallel secondary flow as shown in Fig.10(b), with the accumulation level decreasing with distance from the corner. The higher inertia particles ($St^+ \geq 125$) are driven by the corner-directed secondary flows, and are prone to drift from the highly fluctuating regions (outside the viscous sublayer) into and concentrate in the "stagnation region 1" area of the secondary flow in the duct corner, where the turbulence intensity is low. Moving along the wall away from the "stagnation region 1", the relatively strong wall-parallel secondary flow (regions "B" and "C" marked in yellow) entrains the particles moving them to the middle region of the wall, with this effect weakened with increasing Stokes number. Farther away from the corner, the intensity of the secondary flow is attenuated and the near-wall coherent structures in the buffer layer become responsible for particle motion in this region, including near the second stagnation point of the secondary flow ("stagnation region 2"), where the turbulent fluctuations for the heavier particles are high. Some of the particles in this region will be ejected by these near-wall coherent vortices, and then follow the secondary flow towards the duct centre regions, although most of them tend to remain trapped in the near-wall region similar to what is found in typical wall-bounded turbulence. The particle accumulation rate in the near-corner region can be evaluated by the net particle influx to the corner. In the corner region, inside the blue box ($y^* \leq -0.8, z^* \leq -0.8$) displayed in Fig. 12(a), if the particle influx is much larger than the outflux, particles will gradually accumulate. The particle flux J is defined as the particle number density per unit cell multiplied by the corresponding mean secondary particle velocity. The sign of particle influx is set to be positive, with outflux negative. The mean net normalized particle influx J_{net} versus particle Stokes number in this region is presented in Fig. 12(b). Clearly, the net particle influx first increases with Stokes number and reaches a maximum at $St^+ = 25$, then starts to decline. This trend is in line with the

cross-sectional particle concentrations in Fig.5 and the instantaneous particle distributions in Fig.10.

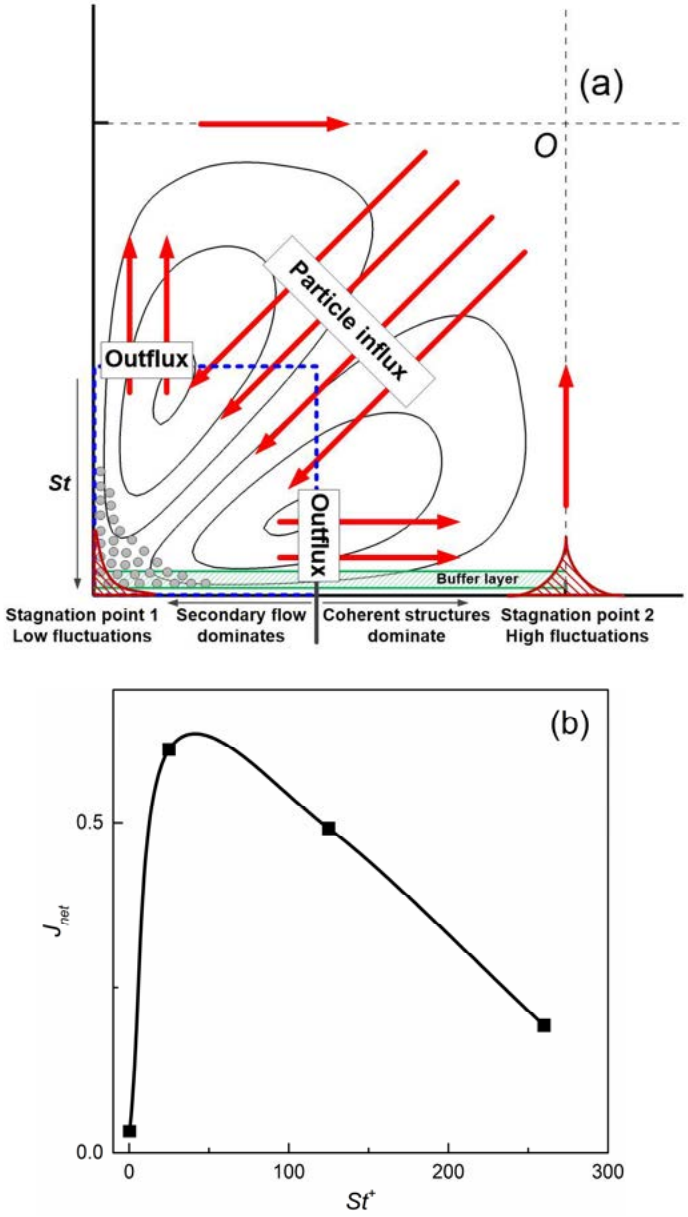

FIG. 12. Mechanism of particle accumulation in the duct cross-section: (a) schematic illustration of the particle secondary motions, and (b) the time-averaged net particle influx versus particle Stokes number in the duct corner region.

3. Flow topology and quadrant analysis

A flow topology and quadrant analysis was further conducted to study the correlation between

particle behaviour and coherent flow structures in the near-wall region, the effects of which were mentioned in relation to Fig. 12(a). According to the approach of Blackburn et al[49], and based on the second and third invariants Q, R of the velocity gradient tensor, topological features in incompressible flows can be categorized into one of four types (see Fig. 14(a)): (I) unstable focus/compressing ($D > 0, R > 0$) and (II) stable focus/stretching ($D > 0, R < 0$), which are two vortical zones, (III) stable node/saddle/saddle ($D < 0, R < 0$) and (IV) unstable node/saddle/saddle ($D < 0, R > 0$), which are two convergence regions, where $D = (27/4)R^2 + Q^3$ is the discriminant of the corresponding characteristic equation of the velocity gradient tensor. In the present duct flow, the flow field was divided into four regions as depicted in Fig.13: the viscous sublayer ($y^+ \leq 5$), the buffer layer ($5 < y^+ \leq 30$), the log-law layer ($30 < y^+ \leq 110$) and the bulk region ($y^+ > 110$). The values of Q, R at each fluid node were computed in each region, and then compared to those sampled at the particle positions to investigate if the particle distribution shows any preference for the different types of local flow topology.

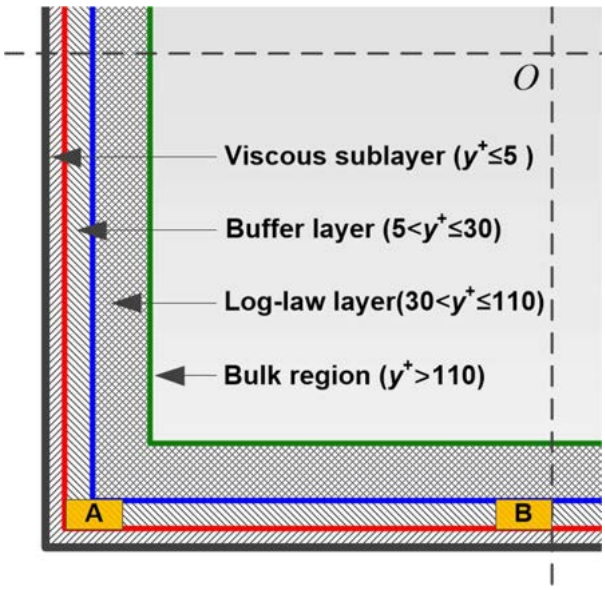

FIG. 13. Schematic diagram of the different regions used for flow topology and quadrant analysis.

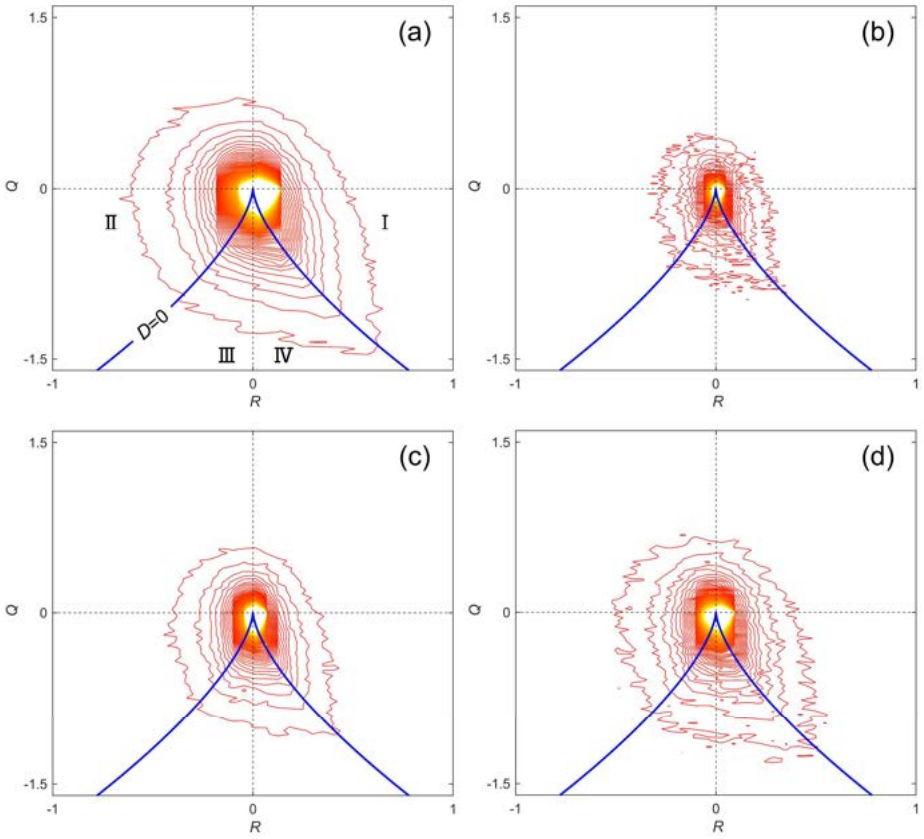

FIG. 14. Joint PDFs of Q, R conditionally sampled at (a) fluid nodes and particle positions in the viscous sublayer for (b) $St^+ = 0.31$, (c) $St^+ = 25$, and (d) $St^+ = 260$ particles.

Figure 14 illustrates the joint PDFs of Q and R in the viscous sublayer sampled at the fluid grid nodes and particle positions for $St^+ = 0.31, 25, 260$, with the same contour levels used for each plot. The PDF at the fluid grid points exhibits a weak preference for the stable focus/stretching (II) and the unstable node/saddle/saddle (IV) topologies, although most of the (Q, R) points lie near the origin, which has also been observed in channel flows[9]. In contrast, the PDFs conditionally sampled at the particle positions show significantly different behaviour. The area enclosed by the PDFs at particle locations in the (Q, R) plane is smaller than that at the fluid nodes, which suggests that these particles tend to avoid the strong vortical regions (topological quadrants I and II) due to the centrifugal effect of the eddies in these regions, with this effect decaying with increasing particle inertia. For the lighter particles with $St^+ = 0.31$, its PDF distribution is almost isotropic, which indicates a weak preferential sampling. The PDF of $St^+ = 25$ particles shows a relatively higher probability both in the stable and the unstable convergence regions, where the particles are likely to

aggregate. The broader PDF distribution observed in Fig. 14(d) for the most inertial $St^+ = 260$ particles indicates a less pronounced preferential concentration of these particles. The flow topology for $St^+ = 125$ particles (not shown) was somewhere in between that of the $St^+ = 25$ and $St^+ = 260$ particles. These results confirm the conclusions regarding particle preferential concentration in the viscous sublayer made in relation to Fig. 5. Overall, the distinct differences between the PDF values of (Q, R) sampled at the particle locations and the fluid nodes implies that the inertial particle's motion is basically decoupled from the coherent structures in the viscous sublayer, where the turbulence level is low and only coherent sweep events associated with the unstable node/saddle/saddle topology play a role[50].

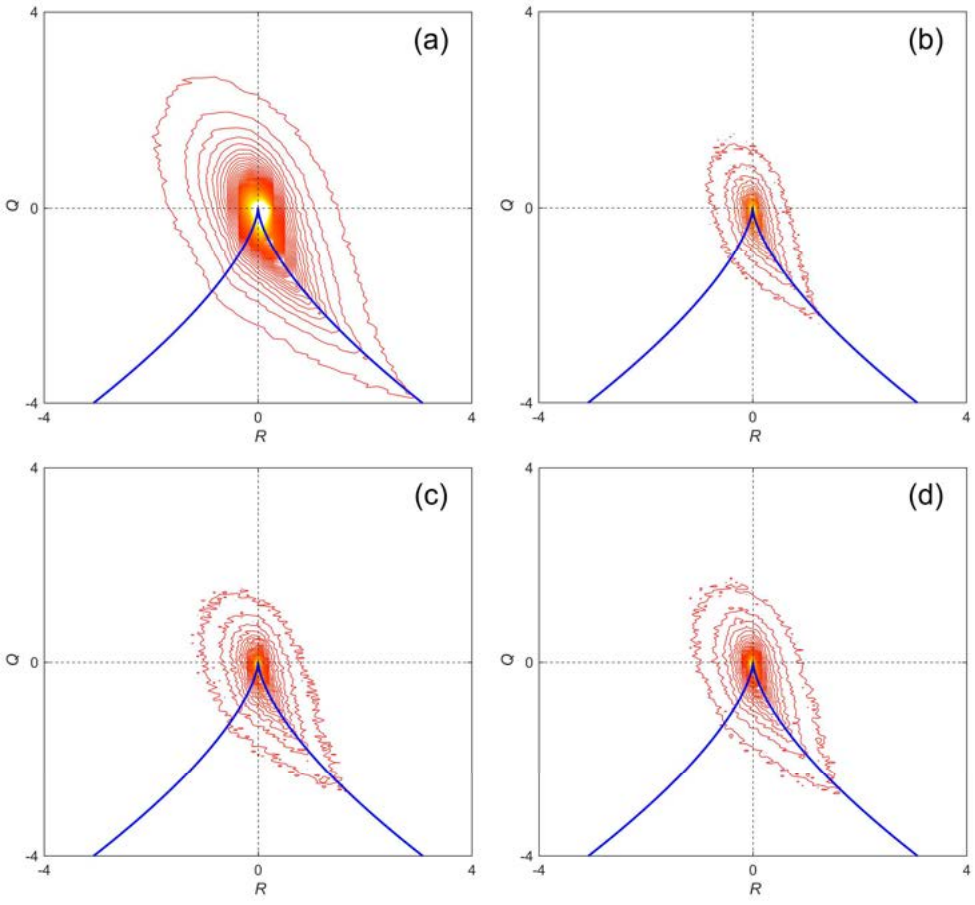

FIG. 15. Joint PDFs of Q, R conditionally sampled at (a) fluid nodes and particle positions in the buffer layer for (b) $St^+ = 0.31$, (c) $St^+ = 25$, and (d) $St^+ = 260$ particles.

Similar plots of the joint PDFs at the fluid nodes and particle positions in the buffer layer are displayed in Fig. 15. It is apparent that the joint PDFs at the fluid grid points in this region show a

much more pronounced preference for the stable focus/stretching and unstable node/saddle/saddle topologies, and similar trends are found in the PDFs of the invariant distribution sampled at the particle positions, suggesting that particles are much more dispersed than in the viscous sublayer. However, the reduction in the size of the invariants at the particle locations still indicates that particles preferentially concentration to some extent, which is mainly due to particle preferential accumulation in the low-speed streaks mentioned earlier in relation to the results of Fig. 6. Concerning the effect of particle inertia, a slightly increasing size of the Q-R distribution with Stokes number is observed in the buffer layer, with this trend similar but less pronounced than the corresponding distributions in the viscous sublayer. This indicates that the inertial particles retain part of the topology characteristics from the buffer layer when they are swept into the vicinity of the wall, although most of the streamwise momentum of the particles is abruptly suppressed during this process.

In the log-law layer, the PDFs of the invariant distribution sampled at the fluid nodes and particle locations (not shown) exhibited a strong resemblance to those in the buffer layer, but showed less dependence on the Stokes number, which is consistent with particle behaviour in channel flows[9,12]. Figure 16 illustrates the same PDFs in the bulk region and, as can be seen, they show a strong preference for the fourth topological quadrant. Furthermore, a pronounced "tear-drop" shape to the Q-R distribution at the fluid grid points is observed in this region. However, in contrast to plane channel flows[9,12], the size of the invariant distribution sampled at the particle locations shows a strong Stokes number dependence in the bulk region, with the smallest size of the Q-R distribution found for $St^+ = 25$ particles. These results are in line with findings in isotropic particle-laden turbulence[1], where mid-inertia particles tend to show the greatest preferential concentration in regions of low vorticity, but lower or higher inertia particles are prone to distribute randomly, which is also in agreement with the results of Bijlard et al[51] for channel flow. This is understandable since turbulence in the duct core regions can be close to homogeneous due to the large distance from the walls, with similar results found by Winkler et al[18] in a square duct flow.

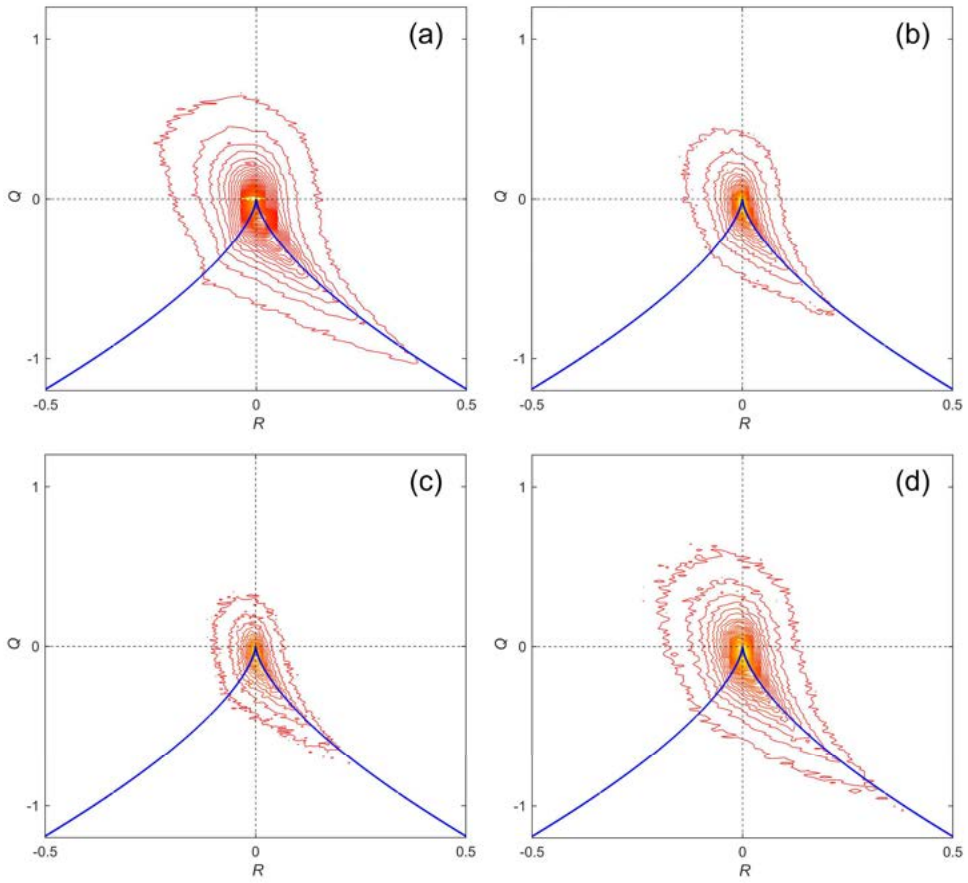

FIG. 16. Joint PDFs of Q, R conditionally sampled at (a) fluid nodes and particle positions in the bulk region for (b) $St^+ = 0.31$, (c) $St^+ = 25$, and (d) $St^+ = 260$ particles.

In addition, it can be noted from Figs. 14-16 that, moving away from the wall from the viscous sublayer to the bulk region, the magnitudes of Q, R at the fluid grid points first increase and then decrease, with the largest scale of the invariant distribution found in the buffer layer, where the turbulence intensity is at its highest[50]. Given that the particle motion is largely unrelated to the coherent structures in the viscous sublayer, the turbulent structures in the buffer layer are mainly responsible for particle behaviour. Chacin and Cantwell[50] found that the preferred flow patterns (unstable focus-compression and unstable node/saddle/saddle) in the lower-right quadrant of the Q-R plane in this region are primarily associated with high Reynolds stress values, which are directly connected to the particle accumulation in the near-wall region. Based on this, a quadrant analysis of the Reynolds stress in the buffer layer was performed in the corner ("A") and wall centre ("B") regions of the duct, as shown in Fig. 13. Figure 17 presents the corresponding joint PDFs of the velocity fluctuations u' (streamwise) and v' (vertical) conditionally sampled at fluid nodes and

particle positions for the $St^+ = 25$ case in these two zones. By comparing Fig. 17(a) with Fig. 17(c), the streamwise fluctuations in the corner region are largely reduced due to the geometrical constraint represented by the sidewalls. Furthermore, it is found that $Q2$, or ejection, events in the corner are important, whereas $Q4$, or sweep, events become dominant on the wall bisector, which is in good agreement with the results of Fornari et al[26]. A similar trend is shared by the PDFs of the velocity fluctuations sampled at the particle locations, but there is a subtle percentage difference in the number of events in each quadrant. Over all the particles considered, the most pronounced ejections in the corner were observed at the locations of the $St^+ = 25$ particles, with the strongest sweeps at the wall bisector also found for these particles, providing an explanation for why these particles show the largest preferential concentration in the near-wall region in Fig. 6.

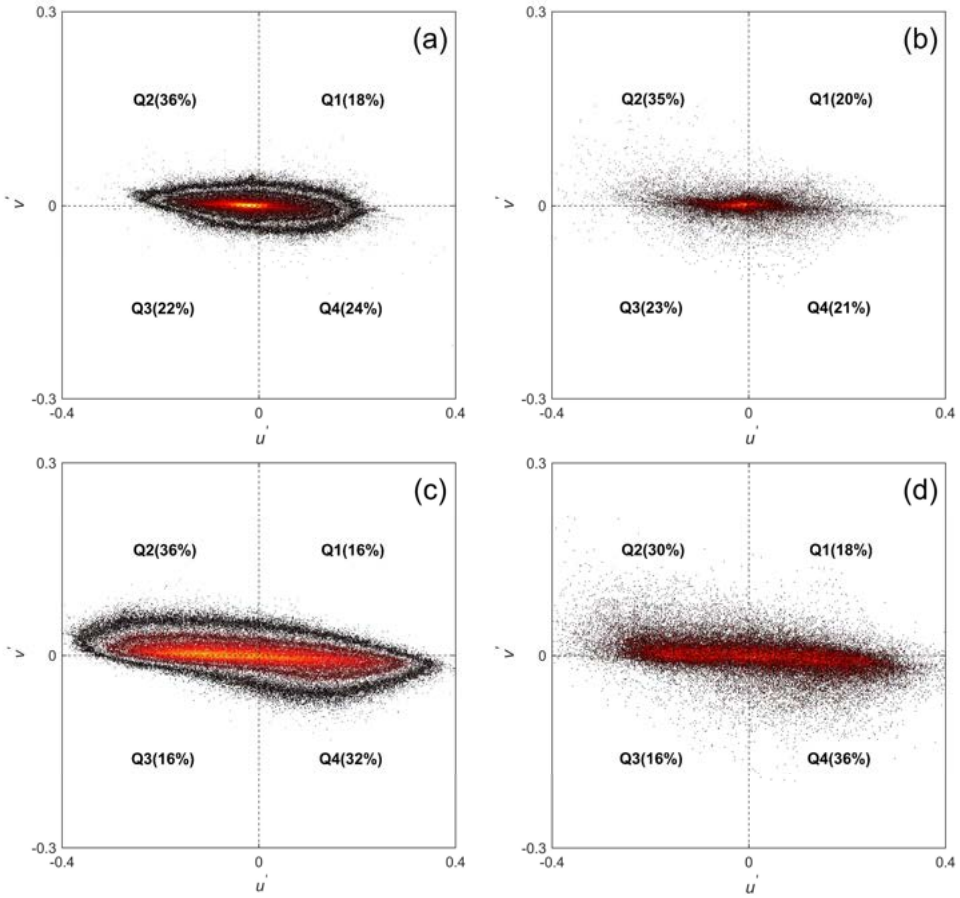

FIG. 17. Joint PDFs of the velocity fluctuations u' and v' conditionally sampled at (a, c) fluid nodes and (b, d) particle positions for particles with $St^+ = 25$ in the (a, b) corner "A" region and (c, d) wall centre region of Fig. 13.

4. Particle dynamic analysis

In this sub-section, more details surrounding the particle dynamics within the duct cross-section are discussed. First of all, the distribution of the averaged cross-sectional drag force for all the considered particles is presented in Fig. 18(a). It is obvious that the average drag force is strong in the near-wall region, with its direction pointing away from the walls, suggesting that the near-wall drag force tends to hinder and decelerate particle motion towards the wall, which partly counteracts the effect of turbophoresis induced by inhomogeneity of the wall-normal turbulence intensity as mentioned earlier. Moving away along the wall centreline towards the duct centre, the magnitude of the drag force gradually declines and reaches a local minimum point where the force changes its direction and turns towards the wall. The position of this minimum point gradually moves inward with increasing particle Stokes number (which can be clearly seen in Fig. 22 considered below). After this point, the magnitude of the drag force first slightly increases and subsequently decreases again as the duct centre is approached. This demonstrates that in the bulk region, the cross-sectional drag force promotes the transport of particles towards the turbulent near-wall regions, although its magnitude is very small. These results are consistent with the findings of Winkler and Rani[52] in a square duct flow and Mortimer et al[12] in channel flow along the wall-normal direction.

Note that the force distribution along the corner bisector is quite distinct for particles with different Stokes numbers. The profiles of the vertical component (F_{dy}^*) of the drag force along the corner bisector for all particles is plotted in Fig. 18(b). Since the vertical and horizontal components of the cross-sectional force are symmetric about the corner bisector, only the vertical component is shown. From this figure, the vertical drag force for particles with $St^+ = 0.31 - 125$ changes its sign at about $y^* = -0.5$ along the bisector. However, there is no change of force direction for the most inertial $St^+ = 260$ particles, which is related to the mean relative motion between the two phases. In fact, according to the definition in Eq. (3), the drag force mainly relies on the relative slip velocity $\vec{u}_s^*$, which directly reflects the extent to which particles follow the local flow. Indeed, cross-sectional contours and profiles of the slip velocity along the corner bisector (not shown) are found to be similar to the force distribution in Fig. 18. Accordingly, particles move faster than the fluid where $F_{dy}^* > 0$ and lag behind the flow where $F_{dy}^* < 0$ (observed in the lower-left quadrant of the duct). For all particles, the maxima of the drag force (in magnitude) along the corner bisector

are located close to the corner, where the secondary velocities of both the fluid and particles reach a peak, as displayed in Fig. 9(b). Except for the low-inertia $St^+ = 0.31$ particles, the secondary velocity of the $St^+ = 125$ particles is closest in magnitude to that of the fluid phase, which results in the relatively small magnitude of the drag force along corner bisector for these particles.

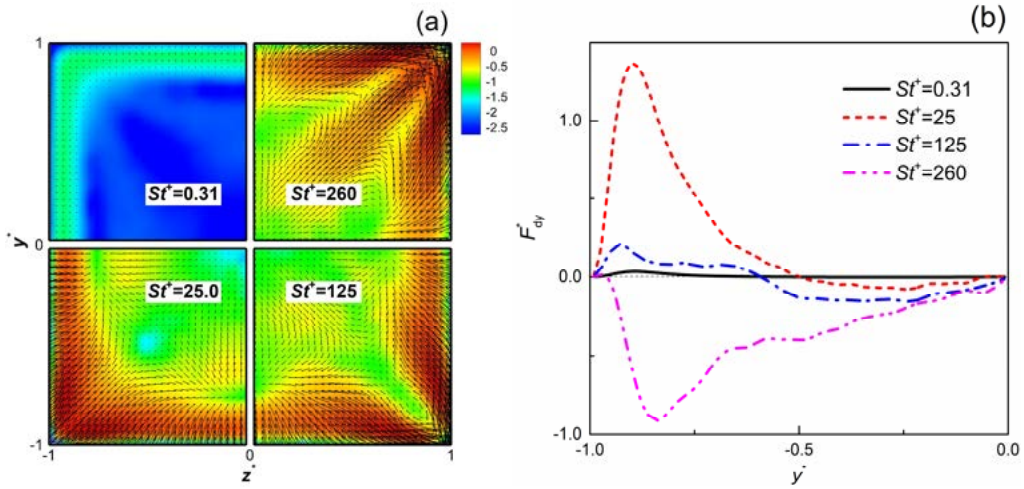

FIG. 18. The non-dimensionalized average cross-sectional drag force for all considered particles: (a) cross-sectional force vectors superimposed with contours of its magnitude (logarithmic values $log_{10}(\sqrt{F_{dy}^{*2} + F_{dz}^{*2}})$), and (b) profiles of the vertical component of the drag force (F_{dy}^{*}) along the corner bisector.

Figure 19 illustrates the distribution of the average cross-sectional lift force and profiles of its vertical component along the corner bisector for all particles considered. It is apparent from Fig. 19(a) that the strongest lift force occurs near the wall, with its direction perpendicular towards the wall. This is in agreement with the results of Wang and Squires[53], who found the most pronounced Saffman lift in the viscous sublayer which is induced by the mean large streamwise velocity gradients in the near-wall region. In Fig. 19(b), outside the viscous sublayer, the magnitude of the lift force for all particles is close to zero, which can thus be neglected. Consequently, in the entire duct cross-section, the lift force only plays an important role in the very near-wall regions, as anticipated, with this force tending to push particles towards the corners and walls of the duct. Further, it is shown from Fig. 19(b) that the magnitude of the shear lift force increases with particle Stokes number in the near-wall region, which can be attributed to increases in the particle-fluid slip velocity. This dependence of the lift force on particle inertia in square duct flows was also observed

by Yao and Fairweather[23] and Winkler and Rani[52].

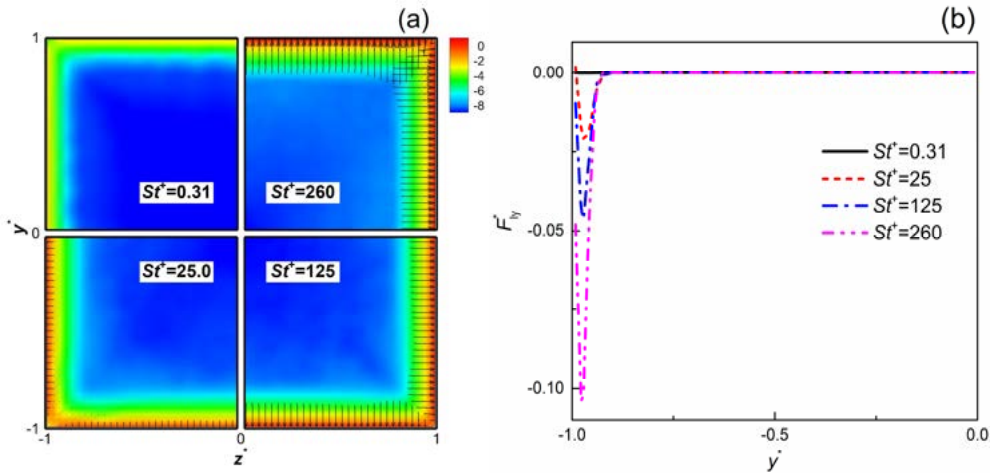

FIG. 19. The non-dimensionalized average cross-sectional lift force for all considered particles: (a) cross-sectional force vectors superimposed with contours of its magnitude (logarithmic values $log_{10}(\sqrt{F_{ly}^{*2} + F_{lz}^{*2}})$), and (b) profiles of the vertical component of the lift force (F_{ly}^{*}) along the corner bisector.

Similar results for the average cross-sectional pressure gradient and virtual mass forces are given in Fig. 20 and Fig. 21, respectively. For the pressure gradient force, Fig. 20(a) shows that the cross-sectional distributions for all particle Stokes numbers behave similarly, and act to push particles away from the walls in the near-wall regions and pull them back towards the walls in the bulk region, with the greatest force magnitude found in the near-wall region because of the large velocity gradients there. The differences in the magnitude of the pressure gradient force between different particles shown in Fig. 20(b) is linked to the varying particle-to-fluid density ratio ρ_p^* used to non-dimensionalize this force. Considering solely the acceleration terms of Eq. (3), it is to be expected that the mean acceleration resulting from the pressure gradient force decreases with particle Stokes number, implying that low-inertia (low particle-fluid density ratio) particles are affected more by this force, which is consistent with the previous investigations of Armenio and Fiorotto[34] and van Hinsberg et al[54] in turbulent flows. In Fig. 21(a), except for the $St^+ = 0.31$ particles, the behaviour of the virtual mass force over the duct cross-section is similar to that of the pressure gradient force. Since the virtual mass force is defined as the difference between the local fluid acceleration and particle acceleration, and for low-inertia particles the magnitude of these two

accelerations is very close, as a result the value of this force is much smaller for low-inertia particles than for high-inertia particles in the near-wall region. As the Stokes number increases, the magnitude of the virtual mass force is also increased, as seen in Fig. 21(b).

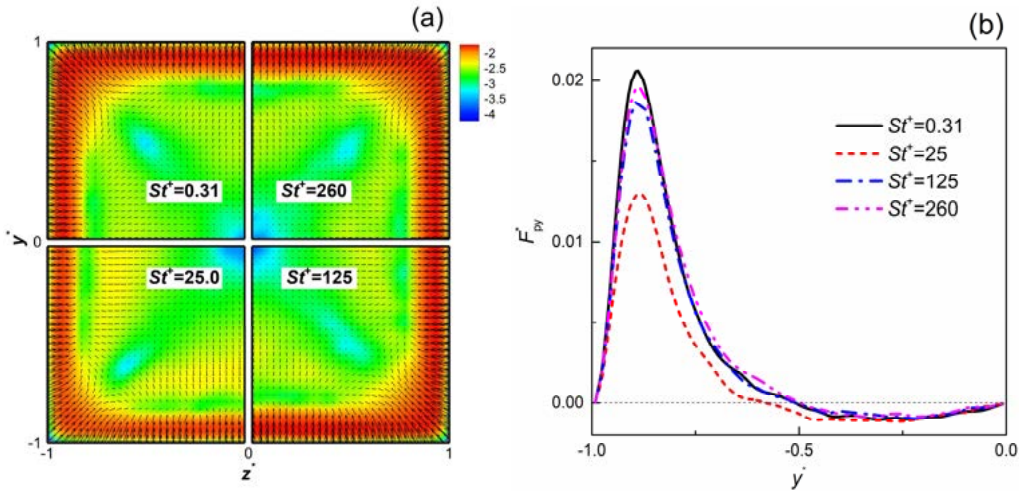

FIG. 20. The non-dimensionalized average cross-sectional pressure gradient force for all considered particles: (a) cross-sectional force vectors superimposed with contours of its magnitude (logarithmic values $log_{10}(\sqrt{F_{py}^{*2} + F_{pz}^{*2}})$), and (b) profiles of the vertical component of the pressure gradient force (F_{py}^{*}) along the corner bisector.

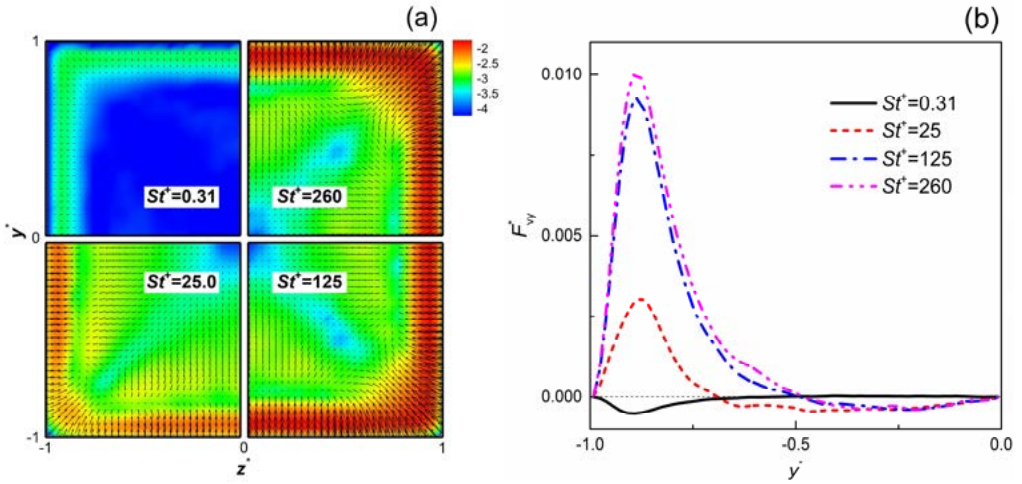

FIG. 21. The non-dimensionalized average cross-sectional virtual mass force for all considered particles: (a) cross-sectional force vectors superimposed with contours of its magnitude (logarithmic values $log_{10}(\sqrt{F_{vy}^{*2} + F_{vz}^{*2}})$), and (b) profiles of the vertical component of the virtual mass force (F_{vy}^{*}) along the corner bisector.

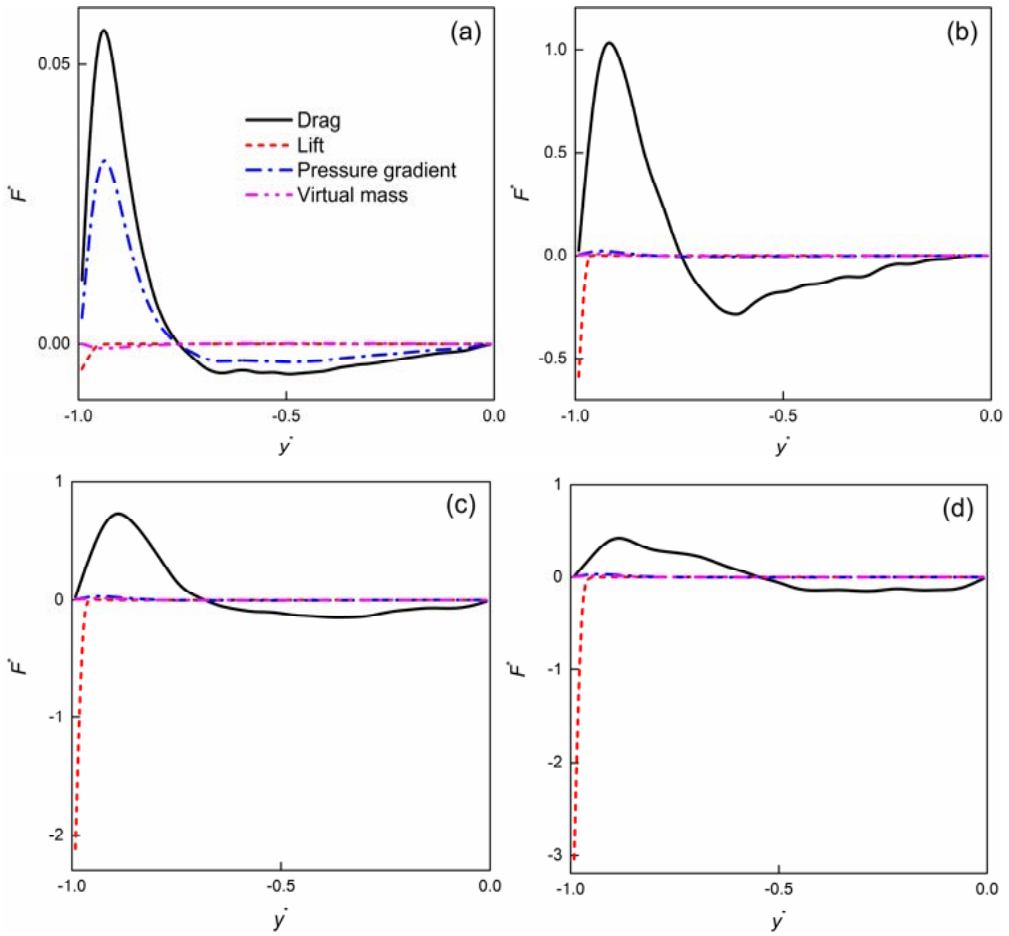

FIG. 22. Comparison between profiles of the vertical component of average cross-sectional values of all forces acting on the particles along the wall bisector for: (a) $St^+ = 0.31$, (b) $St^+ = 25$, (c) $St^+ = 125$, and (d) $St^+ = 260$.

To highlight the relative importance of the various forces for each particle set considered, Fig. 22 provides a comparison of the vertical component of the indicated average forces along the wall bisector. For the low-inertia $St^+ = 0.31$ particles, the particle dynamics are mainly dominated by the drag and pressure gradient forces across the duct cross-section. In the near-wall region, the lift force also plays an important role, with its contribution up to 30% of the drag force. As the particle Stokes number is increased, the lift force becomes more important in the viscous sublayer, with its magnitude even larger than the drag force in the central wall regions for $St^+ \geq 25$ particles. Outside the viscous sublayer, the drag force becomes the only important force and dominates particle motion, with the magnitude of the remaining forces being effectively negligible relative to the drag force in this region. Overall, the resulting average hydrodynamic force acts to repel particles from the walls in the near-wall turbulent regions, while in the bulk region it shows the opposite

trend. Exceptions are in the viscous sublayer for the $St^+ \geq 25$ particles, where the dominant lift force contributes to keep the particles in the near-wall region, which eventually leads to the accumulation of inertial particles in this region.

C. Effect of two-way coupling

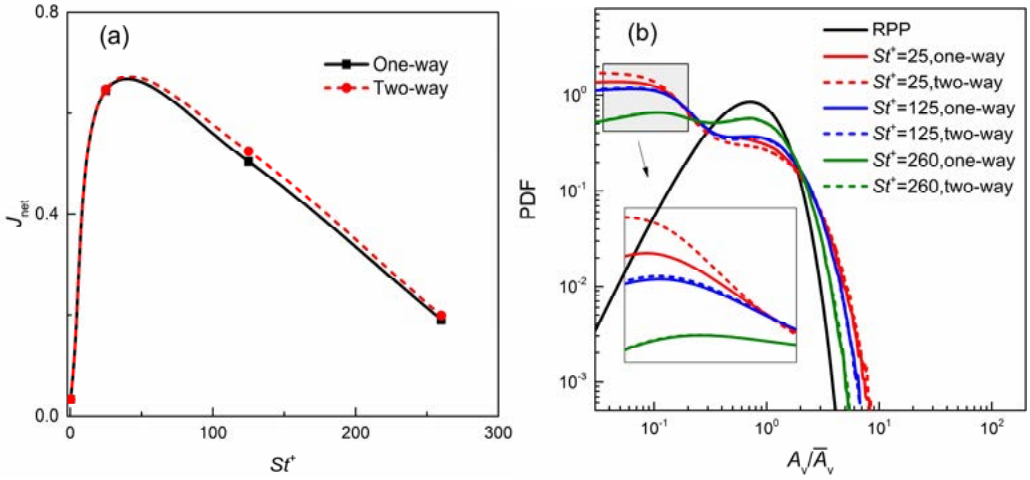

Fig. 23. Comparisons of the effect of one- and two-way coupling on particle accumulation: (a) the time-averaged net particle influx versus particle Stokes number in the duct corner region, and (b) PDFs of the Voronoi cell area compared with a random Poisson distribution in the near-wall region.

Lastly, the impact of enforcing two-way coupling between the particles and the fluid is discussed. For the fluid phase, the presence of particles did not show any effects on the averaged flow statistics at the present low particle volume fraction, although a slight weakening of large-scale vortices and more particle-induced small-scale vortices were observed in the near-wall region of the instantaneous flow field for high-inertia particle sets. Regarding the particle phase, Fig. 23 provides a quantitative comparison of particle accumulation in the duct corner and near-wall regions between one-way and two-way coupling. In Fig. 23(a), the mean net particle influx into the duct corner (previously considered in Fig. 12(b)) under two-way coupling is seen to be slightly higher than in the case of one-way coupling for the $St^+ \geq 25$ particles, revealing that two-way coupling does enhance particle accumulation in the corner region, which is likely, according to Lin et al[25,26], attributable to the intensified secondary flows induced by the addition of particles. The PDFs of the normalized Voronoi cell area in the near-wall regions for $St^+ \geq 25$ particles under the two

conditions is compared in Fig. 23(b). It is observed that PDF values in cluster regions under two-way coupling are slightly larger than for one-way coupling, which indicates that preferential clustering in the near-wall region is also intensified by two-way coupling. This is likely due to the disruption of near-wall quasi-coherent structures by the presence of the particles, which can further result in a reduction of ejection and sweep events[55]. As a consequence, the near-wall streaky structures become more regular and longer, which in turn can cause more concentrated particle preferential accumulation. However, due to the present low particle volume fraction, the effect of two-way coupling is relatively weak, and its dependence on particle inertia is not obvious which hence needs to be further explored using higher particle concentrations.

IV. CONCLUSIONS

Direct numerical simulations of turbulent particle-laden flows in a square duct at $Re_\tau = 300$ have been performed in combination with Lagrangian particle tracking under the conditions of one- and two-way coupling. Four particle population sets with the shear Stokes number St^+ ranging from 0.31-260 have been considered at a fixed particle volume fraction $\emptyset = 10^{-4}$. The aim was to explore the underlying physical mechanisms underpinning particle preferential accumulation induced by the turbulence-driven secondary flows that exist in the turbulent square duct.

In general, inertial particles exhibit strong accumulation near the duct walls as in plane channel flows[12,14]. In particular, due to the effect of the cross-sectional secondary flows, the contour isolines of mean particle concentration bulge slightly towards the duct corner and the heavier particles ($St^+ \geq 25$) more preferentially concentrate in the corner region, with the accumulation level progressively decreasing with increasing Stokes number. The maximum accumulation in the duct corners is observed at a Stokes number of $St^+ = 25$ when the bulk particle Stokes number matches the integral timescale of the mean flow. In the near-wall region, the heavier particles tend to concentrate in low-streamwise-velocity regions and form streamwise-aligned elongated streaks, with this phenomenon most pronounced for the $St^+ = 25$ particles. In the region ($-0.5 < y^*(z^*) < 0.5$) along the wall away from the duct corner where the intensity of the secondary flow is attenuated, near-wall particle accumulation is dominated by the coherent vortices in these regions.

Along the wall bisector, profiles of the mean streamwise velocity for the particle phase are

similar to that in the single-phase channel flow, but indicate that the streamwise particle velocity exceeds that of the fluid in the near-wall region but lags the fluid in the bulk region. The topology of secondary particle vectors in the duct cross-section also resembles that of the fluid phase, but its intensity is strongly influenced by the particle inertia. Along the corner bisector, the magnitude of the secondary particle velocity is observed to first increase then decrease as the Stokes number ranges from 0.31-260, with the maximum achieved at $St^+ = 25$. Furthermore, the greater the intensity of the secondary particle velocity, the further the location of its peak value drifts toward the corner. In the region adjacent to the wall, the intensity of the secondary particle velocity is found to decrease with particle Stokes number. Moreover, in comparison with the fluid phase, the streamwise components of the rms velocity fluctuations for the heavier particles in the cross-section are greatly enhanced, whereas the vertical and spanwise components are correspondingly suppressed. In addition, it is observed that in the near-corner inside the buffer layer, the accumulation patterns for the mid-inertia particles ($St^+ = 25$) tend to follow the streamlines of the mean secondary motions, while the higher inertia particles are more prone to enter and be trapped in the stagnation region of the secondary flow.

Results from a region-based flow topology analysis indicate that the behaviour of the heavier particles decouples from the coherent structures in the viscous sublayer, but can still retain part of the information of topological characteristics from the most turbulent buffer layer, which ultimately leads to preferential concentration in the convergence regions of the viscous sublayer. In the buffer layer close to the duct corner, the flow streamwise fluctuations are largely reduced due to the sidewall constraint, and the particle accumulation here is mainly dominated by $Q2$ events. In contrast, in the region near the wall centre, both $Q2$ and $Q4$ events are important, with the highest Reynolds stress values found at the locations of the $St^+ = 25$ particles, providing the mechanism responsible for particle accumulation mostly occurring in the near-wall region. In the bulk region, the size of the invariant distribution sampled at the particle locations exhibits a strong Stokes number dependence, which is similar to that found in isotropic particle-laden turbulence.

A deeper analysis of the particle dynamics in the duct cross-section shows that the average cross-sectional drag, pressure gradient and virtual mass forces act to repel the heavier particles away from the walls in the near-wall region but tend to drive them back towards the walls in the bulk region, although the magnitude of these forces in the latter region is quite small in comparison with

the near-wall region. One exception is the drag force for the heaviest ($St^+ = 260$) particles along the corner bisector, where their cross-sectional motion largely lags the fluid phase due to their high inertia, which causes the drag force acting on them to always be directed towards the corner. In contrast, the shear lift force only plays an important role in the viscous sublayer, tending to push particles towards the corners and walls of the duct. Regarding the relative importance of the various forces, the drag and pressure gradient forces are primarily responsible for the cross-sectional motion of the low-inertia ($St^+ = 0.31$) particles, whereas the lift force becomes progressively more dominant in the viscous sublayer as the particle Stokes number is increased. For the heavier particles outside the viscous sublayer, the drag force is the only important force and dominates the particle motion, with the other forces being negligible compared to the drag force in this region.

Concerning interactions between the two phases, the inclusion of the point-source-in-cell two-way coupling mechanism is found to slightly enhance particle accumulation in the corner and the near-wall regions, but this effect is very weak at the present low particle volume fraction. Simulations with higher particle concentrations hence need to be further conducted to investigate turbulence modulation by the inertial particles and its effect on particle preferential concentration in turbulent square duct flows.

ACKNOWLEDGMENTS

The authors gratefully acknowledge the financial support from the China Scholarship Council. The computations were performed on the ARC facilities of HPC services provided by the University of Leeds.

REFERENCES

[1] K. D. Squires and J. K. Eaton, “Preferential concentration of particles by turbulence,” Phys. Fluids 3, 1169 (1991).

[2] J. R. Fessler, J. D. Kulick, and J. K. Eaton, “Preferential concentration of heavy particles in a turbulent channel flow,” Phys. Fluids 6, 3742 (1994).

[3] A. M. Wood, W. Hwang, and J. K. Eaton, “Preferential concentration of particles in homogeneous and isotropic turbulence,” Int. J. Multiphase Flow 31, 1120 (2005).

[4] S. Goto and J. C. Vassilicos, “Self-similar clustering of inertial particles and zero-acceleration points

in fully developed two-dimensional turbulence," Phys. Fluids 18, 115103 (2006).

[5] S. W. Coleman and J. C. Vassilicos, "A unified sweep-stick mechanism to explain particle clustering in two- and three-dimensional homogeneous, isotropic turbulence," Phys. Fluids 21, 113301 (2009).

[6] M. Obligado, T. Teitelbaum, A. Cartellier, P. Mininni, M. Bourgoin, "Preferential concentration of heavy particles in turbulence," J. Turbul. 15, 293 (2014).

[7] M.W. Reeks, "The transport of discrete particles in inhomogeneous turbulence," J. Aerosol Sci. 14, 729 (1983).

[8] C. Narayanan, D. Lakehal, L. Botto, A. Soldati, "Mechanisms of particle deposition in a fully developed turbulent open channel flow," Phys. Fluids 15, 763 (2003).

[9] D. Rouson and J. Eaton, "On the preferential concentration of solid particles in turbulent channel flow," J. Fluid Mech. 428, 149 (2001).

[10] C. Marchioli and A. Soldati, "Mechanisms for particle transfer and segregation in a turbulent boundary layer," J. Fluid Mech. 468, 283 (2002).

[11] A. Soldati and C. Marchioli, "Physics and modelling of turbulent particle deposition and entrainment: Review of a systematic study," Int. J. Multiphase Flow 35, 827 (2009).

[12] L. F. Mortimer, D. O. Njobuenwu and M. Fairweather, "Near-wall dynamics of inertial particles in dilute turbulent channel flows," Phys. Fluids 31, 063302 (2019).

[13] A. G. Kidanemariam, C. Chan-Braun, T. Doychev, M. Uhlmann, "Direct numerical simulation of horizontal open channel flow with finite-size, heavy particles at low solid volume fraction," New J. Phys. 15, 025031 (2013).

[14] G. Sardina, P. Schlatter, L. Brandt, F. Picano, C. M. Casciola, "Wall accumulation and spatial localization in particle laden wall flows," J. Fluid Mech. 699, 50 (2012).

[15] A. Pinelli, M. Uhlmann, A. Sekimoto, G. Kawahara, "Reynolds number dependence of mean flow structure in square duct turbulence," J. Fluid Mech. 644, 107 (2010).

[16] R. Vinuesa, A. Noorani, A. Lozanodurán, G.K. El Khoury, P. Schlatter, P. F. Fischer, H. M. Nagib, "Aspect ratio effects in turbulent duct flows studied through direct numerical simulation," J. Turbul. 15, 677 (2014).

[17] S. Pirozzoli, D. Modesti, P. Orlandi, F. Grasso, "Turbulence and secondary motions in square duct flow," J. Fluid Mech. 840, 631 (2018).

[18] C.M. Winkler, Sarma L. Rani and S.P. Vanka, "Preferential concentration of particles in a fully

developed turbulent square duct flow," Int. J. Multiphase Flow 30, 27 (2004).

[19] G. Sharma and D.J. Phares, "Turbulent transport of particles in a straight square duct," Int. J. Multiphase Flow 32, 823 (2006).

[20] M. Fairweather and J. Yao, "Mechanisms of particle dispersion in a turbulent, square duct flow," AIChE J. 55, 1667 (2009).

[21] D. J. Phares and G. Sharma, "A DNS study of aerosol deposition in a turbulent square duct flow," Aerosol Sci. Tech. 40, 1016 (2006).

[22] C.M. Winkler, S. L. Rani and S.P. Vanka, "A numerical study of particle wall-deposition in a turbulent square duct flow," Powder Tech. 170, 12 (2006).

[23] J. Yao and M. Fairweather, "Particle deposition in turbulent duct flows," Chem. Eng. Sci. 84, 781 (2012).

[24] A. Noorani, R. Vinuesa, L. Brandt, P. Schlatter, "Aspect ratio effect on particle transport in turbulent duct flows," Phys. Fluids 28, 115103 (2016).

[25] Z. Lin, Z. Yu, X. Shao, L. Wang, "Effects of finite-size neutrally buoyant particles on the turbulent flows in a square duct," Phys. Fluids 29, 103304 (2017).

[26] W. Fornari, H.T. Kazerooni, J. Hussong, L. Brandt, "Suspensions of finite-size neutrally buoyant spheres in turbulent duct flow," J. Fluid Mech. 851, 148 (2018).

[27] S. Zade, W. Fornari, F. Lundell, L. Brandt, "Buoyant finite-size particles in turbulent duct flow," Phys. Rev. Fluids 4, 024303 (2019).

[28] W. Fornari, A. Formenti, F. Picano, L. Brandt, "The effect of particle density in turbulent channel flow laden with finite size particles in semi-dilute conditions," Phys. Fluids 28, 033301 (2016).

[29] S.K. Robinson, "Coherent motions in the turbulent boundary layer," Annu. Rev. Fluid Mech. 23, 601 (1991).

[30] J. Jiménez and S. Hoyas, "Turbulent fluctuations above the buffer layer of wall-bounded flows," J. Fluid Mech. 611, 215 (2010).

[31] P. F. Fischer, J. W. Lottes, and S. G. Kerkemeier, Nek5000, http://nek5000.mcs. anl.gov, 2008.

[32] G. K. El Khoury, P. Schlatter, A. Noorani, P. F. Fischer, G. Brethouwer, and A. V. Johansson, "Direct numerical simulation of turbulent pipe ow at moderately high Reynolds numbers," Flow Turbul. Combust. 91, 475 (2013).

[33] M. R. Maxey, and J. J. Riley, "Equation of motion for a small rigid sphere in a nonuniform flow," Phys.

Fluids 26, 883 (1983).

[34] V. Armenio, and V. Fiorotto, “The importance of the forces acting on particles in turbulent flows,” Phys. Fluids 13, 2437 (2001).

[35] Y. Pan and S. Banerjee, “Numerical simulation of particle interactions with wall turbulence,” Phys. Fluids 8, 2733 (1996).

[36] A. Daitche, “On the role of the history force for inertial particles in turbulence,” J. Fluid Mech., 782, 567 (2015).

[37] L. Zeng, F. Najjar, S. Balachandar, P. Fischer, “Forces on a finite-sized particle located close to a wall in a linear shear flow,” Phys. Fluids 21, 033302 (2009).

[38] M. W. Schmeeckle, J. M. Nelson, R. L. Shreve, “Forces on stationary particles in near-bed turbulent flows,” J. Geophys. Res. 112, F02003 (2007).

[39] C. Jin, I. Potts, M. W. Reeks, “The effects of near wall corrections to hydrodynamic forces on particle deposition and transport in vertical turbulent boundary layers,” Int. J. Multiphase Flow 79, 62 (2016).

[40] L. Schiller, and A. Naumann, “Fundamental calculations in gravitational processing,” Z. Ver. Dtsch. Ing. 77, 318 (1933).

[41] G. Sardina, F. Picano, P. Schlatter, L. Brandt, C. M. Casciola, “Statistics of particle accumulation in spatially developing turbulent boundary layers,” Flow, Turbul. Combust. 92, 27 (2014).

[42] R. Monchaux, M. Bourgoin, A. Cartellier, “Preferential concentration of heavy particles: A Voronoï analysis,” Phys. Fluids 22, 033302 (2010).

[43] C. Nilsen, H. I. Andersson, L. Zhao, “A Voronoi analysis of preferential concentration in a vertical channel flow,” Phys. Fluids 25, 115108 (2013).

[44] X. Liu, C. Ji, X. Xu, D. Xu, J. J.R. Williams, “Distribution characteristics of inertial sediment particles in the turbulent boundary layer of an open channel flow determined using Voronoi analysis,” Int. J. Sediment Res. 32, 401 (2017).

[45] J. Ferenc, Z. Néda, “On the size distribution of Poisson Voronoi cells,” Physica A. 385, 518 (2007).

[46] K. T. Kiger and C. Pan, “Suspension and turbulence modification effects of solid particulates on a horizontal turbulent channel flow,” J. Turb. 3, 1 (2002).

[47] M. Righetti and G. P. Romano, “Particle- fluid interactions in a plane near-wall turbulent flow,” J. Fluid Mech. 505, 93 (2004).

[48] J. Kulick, J. Fessler, J. Eaton, “Particle response and turbulence modification in fully developed channel

flow," J. Fluid Mech. 277, 109 (1994).

[49] H. M. Blackburn, N. N. Mansour, B. J. Cantwell, "Topology of fine-scale motions in turbulent channel flow," J. Fluid Mech. 310, 269 (1996).

[50] J. M. Chacin and B. J. Cantwell, "Dynamics of a low Reynolds number turbulent boundary layer," J. Fluid Mech. 404, 87 (2000)

[51] M. Bijlard, R. Oliemans, L. Portela, G. Ooms, "Direct numerical simulation analysis of local flow topology in a particle-laden turbulent channel flow," J. Fluid Mech. 653, 35 (2010).

[52] C.M. Winkler and S. L. Rani, "A Relative importance of the lift force on heavy particles due to turbulence driven secondary flows," Powder Tech. 190, 310 (2009).

[53] Q. Wang, K. Squires, "Large eddy simulation of particle deposition in a vertical turbulent channel flow," Int. J. Multiphase Flow 22, 667 (1996).

[54] M.A.T. van Hinsberg, H.J. Clercx, F. Toschi, "Enhanced settling of nonheavy inertial particles in homogeneous isotropic turbulence: The role of the pressure gradient and the Basset history force," Phys. Rev. E. 95, 023106 (2017).

[55] L. H. Zhao, H. I. Andersson, and J. J. J. Gillissen, "Turbulence modulation and drag reduction by spherical particles," Phys. Fluids 22, 081702 (2010).